Cryo-EM Structures of Respiratory bc_1-cbb_3 type $CIII_2CIV$ Supercomplex and Electronic Communication Between the Complexes

Stefan Steimle[1], Trevor VanEeuwen[2], Yavuz Ozturk[1,#], Hee Jong Kim[2], Merav Braitbard[3], Nur Selamoglu[1], Benjamin A. Garcia[4], Dina Schneidman-Duhovny[3], Kenji Murakami[4,*] and Fevzi Daldal[1,*]

[1]Department of Biology, University of Pennsylvania, Philadelphia, PA, 19104; [2]Biochemistry and Molecular Biophysics Graduate Group, Perelman School of Medicine, University of Pennsylvania, Philadelphia, PA 19104; [#]Institute of Biochemistry and Molecular Biology, Faculty of Medicine, Albert-Ludwigs University of Freiburg, 79104 Freiburg, Germany; [3]School of Computer Science and Engineering, Institute of Life Sciences, The Hebrew University of Jerusalem, Jerusalem, 9190401, Israel and [4]Department of Biochemistry and Biophysics, Perelman School of Medicine, University of Pennsylvania, Philadelphia, PA 19104

Running title: Bacterial respiratory cytochrome bc_1-cbb_3 supercomplex

Key words: cytochrome bc_1 or Complex III; Cytochrome cbb_3 oxidase or Complex IV; respiratory supercomplex; electron carrier cytochrome *c*: membrane-anchored cytochrome c_y; soluble cytochrome c_2; *Rhodobacter capsulatus*; respiratory electron transport chain

***Corresponding authors**: Fevzi Daldal: fdaldal@sas.upenn.edu
Phone: +1 215 898-4394

Kenji Murakami: kenjim@pennmedicine.upenn.edu
Phone: +1 215 573-1125

Abbreviations

Q, quinone; QH_2, Quinol or hydroquinone; Complex III, $CIII_2$ or cytochrome bc_1, ubiquinol-cytochrome *c* oxidoreductase; Complex IV or CIV, cbb_3-type cytochrome *c* oxidase; cyt, cytochrome; cyt c_2, cytochrome c_2, soluble cytochrome *c*; cyt c_y, cytochrome c_y, membrane-anchored cytochrome *c*; cyt S-c_y, soluble part of cytochrome c_y without its membrane anchor; SC, super-complex; MS, mass spectrometry; XL-MS, cross-linking mass spectrometry; XL, cross-links; TMBZ, 3,3',5,5'-tetramethyl-benzidine; DBH_2, 2,3-dimethoxy-5-methyl-6-*decyl*-1,4-*benzoquinone*; FeS, Rieske iron-sulfur protein; FeS-ED, membrane-extrinsic domain of FeS protein; b position, location of the [2Fe-2S] cluster near heme b_L; c position, location of the [2Fe-2S] cluster near heme c_1; cryo-EM, cryogenic electron microscopy; BN-PAGE, blue native polyacrylamide gel electrophoresis; SDS-PAGE, sodium dodecylsulfate polyacrylamide gel electrophoresis; C-ter, C-terminus; N-ter, N-terminus; His-tag, 8-histidine tag; FLAG-tag, DYKDDDDK-tag; SEC, size exclusion chromatography; TMH, transmembrane helix; DSS, disuccinimidyl suberate; DSBU, disuccinimidyl dibutyric urea; DMTMM, 4-(4,6-dimethoxy-1,3,5-triazin-2-yl)-4-methyl-morpholinium chloride; heme-Fe, heme-iron; E_m, redox midpoint potential; heme c_{p1}, N-ter located *c*-type heme 1 of CcoP; heme c_{p2}, C-ter located *c*-type heme 2 of CcoP; heme c_o, *c*-type heme of CcoO; SO_3^{2-}, sulfite; SO_4^{2-}, sulfate; RMSD, root-mean-square deviation; DDM, n-dodecyl β-D-maltoside.

Abstract

The respiratory electron transport complexes convey electrons from nutrients to oxygen and generate a proton-motive force used for energy (ATP) production in cells. These enzymes are conserved among organisms, and organized as individual complexes or combined forming large super-complexes (SC). Bacterial electron transport pathways are more branched than those of mitochondria and contain multiple variants of such complexes depending on their growth modes. The Gram-negative species deploy a mitochondrial-like cytochrome bc_1 (Complex III, $CIII_2$), and may have bacteria-specific cbb_3-type cytochrome *c* oxidases (Complex IV, CIV) in addition to, or instead of, the canonical aa_3-type CIV. Electron transfer between these complexes is mediated by two different carriers: the soluble cytochrome c_2 which is similar to mitochondrial cytochrome *c* and the membrane-anchored cytochrome c_y which is unique to bacteria. Here, we report the first cryo-EM structure of a respiratory bc_1-cbb_3 type SC ($CIII_2CIV$, 5.2Å resolution) and several conformers of native $CIII_2$ (3.3Å resolution) from the Gram-negative bacterium *Rhodobacter capsulatus*. The SC contains all catalytic subunits and cofactors of $CIII_2$ and CIV, as well as two extra transmembrane helices attributed to cytochrome c_y and the assembly factor CcoH. Remarkably, some of the native $CIII_2$ are structural heterodimers with different conformations of their [2Fe-2S] cluster-bearing domains. The unresolved cytochrome *c* domain of c_y suggests that it is mobile, and it interacts with $CIII_2CIV$ differently than cytochrome c_2. Distance requirements for electron transfer suggest that cytochrome c_y and cytochrome c_2 donate electrons to heme c_{p1} and heme c_{p2} of CIV, respectively. For the first time, the $CIII_2CIV$ architecture and its electronic connections establish the structural features of two separate respiratory electron transport pathways (membrane-confined and membrane-external) between its partners in Gram-negative bacteria.

Introduction

Mitochondrial and bacterial respiratory chains couple exergonic electron transport from nutrients to the terminal acceptor oxygen (O_2) through a set of enzyme complexes. Concomitantly, they generate a proton motive force used for ATP synthesis and other energy-dependent cellular processes. The mitochondrial respiratory chain consists of four complexes. Complex I (NADH dehydrogenase) and Complex II (succinate dehydrogenase) are the entry points of reducing equivalents (NADH and $FADH_2$) derived from nutrients into the chain. They reduce the hydrophobic electron carrier quinone (Q). Reduced quinone (QH_2) moves rapidly within the membrane to Complex III (cytochrome (cyt) bc_1 or $CIII_2$) which oxidizes it and reduces the electron carrier cyt *c*. The reduced cyt *c* diffuses to Complex IV (cyt *c* oxidase or CIV) which oxidizes it and subsequently reduces the terminal electron acceptor oxygen to water (Nicholls and Ferguson, 2013) (**Fig. 1A**).

Respiratory complexes are evolutionarily conserved among organisms, but bacterial enzymes are structurally simpler than their mitochondrial counterparts, consisting mainly of the catalytic subunits. However, bacterial respiratory chains are more elaborate than those of mitochondria, since they contain various complexes forming branched pathways to accommodate their diverse growth modes (Melo and Teixeira, 2016). In facultative phototrophs, the mitochondrial-like bc_1-type $CIII_2$ is central to respiratory and photosynthetic electron transport pathways. $CIII_2$ is a dimer with each monomer comprised of three subunits: the Rieske FeS (FeS) protein with a [2Fe-2S] cluster, cyt *b* with hemes b_H and b_L, and cyt c_1 with heme c_1 cofactors (**Fig. 1A,B**). The FeS protein external domain (FeS-ED) is mobile between the **b** (close to heme b_L) and **c** (close to heme c_1) positions (Darrouzet et al., 2001; Esser et al., 2006). Some species such as *Rhodobacter sphaeroides* contain a mitochondrial-like aa_3-type and a bacteria-specific cbb_3-type CIV, a monomer comprised of four subunits: CcoN with heme *b* and heme b_3-Cu binuclear center, CcoO with heme c_o, CcoQ, and CcoP with hemes c_{p1} and c_{p2} cofactors (**Fig. 1A,B**). Other species such as *Rhodobacter capsulatus* (Khalfaoui-Hassani et al., 2016)

and pathogens like *Helicobacter pylori* and *Campylobacter jejuni* (Smith et al., 2000), *Neisseria* (Aspholm et al., 2010) have only a high oxygen affinity cbb_3-type CIV to support their micro-aerophilic growth.

Besides the mitochondrial-like soluble and diffusible cyt *c*, many Gram-negative bacteria contain additional electron carriers that are membrane-anchored via transmembrane domains (*e.g.*, *Rhodobacter capsulatus* cyt c_y (Jenney and Daldal, 1993), *Paracoccus denitrificans* cyt c_{552} (Turba et al., 1995), and *Bradyrhizobium japonicum* CycM (Bott et al., 1991)) or fatty acids (*e.g.*, *Blastochloris viridis* tetraheme cyt *c* (Weyer et al., 1987) and *Helicobacterium gestii* cyt c_{553} (Albert et al., 1998)). Conversely, Gram-positive bacteria are devoid of freely diffusing electron carriers. Instead, they may have additional cyt *c* domains fused to their $CIII_2$ (*i.e.*, *bcc*-type) such as in *Mycobacterium smegmatis* (Kim et al., 2015) and *Corynebacterium glutamicum* (Niebisch and Bott, 2003) or CIV (*i.e.*, caa_3-type) such as in *Bacillus subtilis* (Winstedt and von Wachenfeldt, 2000) and *Bacillus stearothermophilus* (Sakamoto et al., 1996). Bacterial electron carrier cyts *c* are involved in multiple metabolic pathways. Both the diffusible cyt *c* (*e.g.*, *R. capsulatus* cyt c_2 or its homologs) and the membrane-anchored cyt *c* (*e.g.*, *R. capsulatus* c_y or its homologs) electronically connect $CIII_2$ to the photochemical reaction center in photosynthesis (Daldal et al., 1986), and to CIV in respiration (Hochkoeppler et al., 1995). In species like *R. sphaeroides,* cyt c_2 functions in both photosynthesis and respiration, while cyt c_y is restricted to respiration (Myllykallio et al., 1999).

In recent years, the co-occurrence of individual complexes together with multi-enzyme super-complexes (SCs) in energy-transducing membranes has become evident (Acin-Perez and Enriquez, 2014; Melo and Teixeira, 2016). However, the regulation and physiological role of this heterogeneity are debated (Brzezinski, 2019; Letts and Sazanov, 2017; Milenkovic et al., 2017). SCs may stabilize individual complexes, enhance catalytic efficiency through substrate/product channeling, or minimize production of harmful intermediates (*e.g.*, reactive oxygen species) to decrease cellular distress

(Enriquez, 2016; Letts et al., 2019; Quintana-Cabrera and Soriano, 2019). Mitochondrial SCs, such as $CICIII_2CIV$ (respirasomes) or their smaller variants containing only $CICIII_2$ (Sousa and Vonck, 2019) or $CIII_2CIV$ (Letts et al., 2016) have established molecular architectures (Gu et al., 2016; Hartley et al., 2019; Wu et al., 2016). Bacterial SCs, including these of *P. denitrificans* (Berry and Trumpower, 1985; Stroh et al., 2004), *Geobacillus stearothermophilus* (Bergdoll et al., 2016), *Bacillus PS3* (Sone et al., 1987), *M. smegmatis* (Kim et al., 2015), and *C. glutamicum* (Kao et al., 2016), have been characterized biochemically, but only the structure of the Gram positive *M. smegmatis* SC ($CIII_2CIV_2$) has been reported (Gong et al., 2018; Wiseman et al., 2018).

As of yet, no respiratory SC structure has been determined for Gram-negative bacteria, the evolutionary precursors of mitochondria. Furthermore, SCs containing ancient forms of CIV (*i.e.*, cbb_3-type) representing primordial features of respiratory chains with multiple electron carriers are unknown (Ducluzeau et al., 2008). Structural studies of such SCs have been hampered due to unstable interaction between $CIII_2$ and CIV, hence their trace amounts in nature. We have overcome this hurdle using a genetic approach, yielding large amounts of SCs from the Gram negative facultative phototroph *R. capsulatus*. Here, we report the first cryo-EM structure of a respiratory bc_1-cbb_3 type SC ($CIII_2CIV$, at 5.2Å resolution), as well as several conformers of native $CIII_2$ (at 3.3-4.2Å resolution). We define the interaction regions of cyt c_2 and cyt c_y within the SC by combining cryo-EM, cross-linking mass spectrometry (XL-MS) and integrative structure modeling. We propose that the membrane-bound cyt c_y donates electrons to heme c_{p1}, while the diffusible cyt c_2 transfers them to heme c_{p2}, of CcoP subunit of CIV. For the first time, this work establishes the structural features of $CIII_2CIV$ and its two distinct respiratory electron transport pathways (membrane-confined and membrane-peripheral) connecting its partners in Gram-negative bacteria.

Results

Stabilization, isolation, and composition of functional fused SCs. Earlier studies on soluble cyt *c*-independent electron transport pathways have indicated that in some species (*e.g.*, *R. capsulatus* (Myllykallio et al., 2000)), $CIII_2$, CIV, and the membrane-anchored cyt c_y are in close proximity to each other. BN-PAGE of membranes from a wild type strain of *R. capsulatus*, overstained for CIV-specific in-gel activity, showed barely detectable bands around ~450 kDa M_r (**Fig. S1A**). The masses of these bands were larger than that of the CIV monomer (~100 kDa, running as ~230 kDa on BN-PAGE) or $CIII_2$ dimer (~200 kDa, running as >250 kDa on BN-PAGE), suggesting the occurrence of large SCs. However, these entities were of low abundance and highly unstable, rendering their study difficult. In our earlier work, translationally fusing cyt c_1 of $CIII_2$ to cyt c_y had produced an active *bcc*-type $CIII_2$ (*i.e.*, cyt bc_1-c_y fusion) (Lee et al., 2008), suggesting that this approach might also be used to stabilize the interactions between $CIII_2$ and CIV.

During the assembly processes of $CIII_2$ and CIV, cyt c_1 interacts with cyt *b* to form a cyt *b*-c_1 subcomplex (Davidson et al., 1992), and CcoP associates with CcoNOQ subcomplex to yield an active CIV (Kulajta et al., 2006). We thought that translationally fusing the C-terminus (C-ter) of cyt c_1 to the N-terminus (N-ter) of CcoP, which are on the inner (*n*) side of the membrane, forming a bipartite cyt c_1-CcoP fusion protein might produce a stable bipartite bc_1-cbb_3 type SC (left panels of **Fig. 1C,D**). Furthermore, adding the natural 69-residue linker (L) and the 100-residue cyt *c* domain of c_y to the C-ter of cyt c_1-CcoP, which is on the outer (*p*) side of the membrane, to form a tripartite cyt c_1-CcoP-c_y fusion protein might yield a tripartite bc_1-$ccbb_3$ type SC with an attached electron carrier (right panels of **Fig. 1C,D**). This approach (see Supplemental Information, Methods, for details) yielded fusion constructs (**Fig. S1B**) that functionally complemented a mutant lacking $CIII_2$ and CIV for photosynthesis-proficiency (*i.e.*, $CIII_2$ activity) and CIV activity (**Fig. S1C**).

The His-tagged bipartite and Flag-tagged tripartite SCs were purified from detergent-dispersed membranes by tag-affinity and size exclusion chromatography (SEC) (SI, Methods) (**Fig. 2A,B**). BN-PAGE of isolated proteins showed that the A-1 and B-1 fractions contained mostly the large entities of M_r ~450 kDa range (**Fig. 2A,B**, insets), and SDS-PAGE revealed that they had the cyt c_1-CcoP (~65 kDa) or cyt c_1-CcoP-c_y fusion proteins (~80 kDa) (**Fig. 2C**). All protein bands seen in **Fig. 2C** were identified by mass spectrometry (MS) (**Table S3**) and assigned to the subunits of $CIII_2$ and CIV. The fusion proteins also contained covalently-attached heme cofactor(s), as shown by 3,3',5,5'-*tetramethyl-benzidine* (TMBZ) staining, which is specific to covalent heme containing *c*-type cyts **(Fig. 2D)**. CcoQ (M_r ~7kDa) of CIV was absent in both SC preparations.

Spectral and functional characterization of SCs. Purified SCs were characterized by optical redox difference spectra for their total cyt *b* and cyt *c* contents. The spectra were distinct from those of $CIII_2$ (Valkova-Valchanova et al., 1998) or CIV (Gray et al., 1994), and the tripartite SC contained more heme *c* than the bipartite SC, due to the additional cyt *c* domain of c_y (**Fig. S2A**). Both SC preparations exhibited 2,3-dimethoxy-5-methyl-6-*decyl*-1,4-*benzoquinone* (DBH_2):cyt *c* reductase activity (12.4 +/-1.8 μmol/mg of protein/min and 7.2 +/-2.1 μmol/mg of protein/min for bipartite and tripartite SCs, respectively), which is specific to bc_1-type $CIII_2$ (**Fig. S2B)**. They also had cyt *c*:O_2 reductase activity (0.46 +/-0.14 μmol/mg of protein/min and 2.9 +/-0.7 μmol/mg of protein/min for bipartite and tripartite SCs, respectively), which is specific to cbb_3-type CIV (**Fig. S2C**). Importantly, the tripartite SC exhibited DBH_2 and O_2 dependent DBH_2:O_2 reductase (*i.e.*, coupled $CIII_2$+CIV) activity (0.143 +/-0.025 μmol of O_2 consumed/mg of protein/min) without addition of a soluble electron carrier (*e.g.*, horse heart cyt *c* or *R. capsulatus* cyt c_2) (**Fig. S2D**), unlike the bipartite SC that required it. Remarkably, the cyt *c* domain of c_y fused to cyt c_1-CcoP transferred electrons from $CIII_2$ to CIV.

Structures of the tripartite SCs. We first focused on cryo-EM analysis of the tripartite SC preparations that were more stable and abundant than the bipartite SCs (**Fig. 2B,** fraction B-1). Initial 3D classes were of primarily two different sizes (**Fig. S3**, Box 1, left). The smaller (~180Å length) particles were asymmetrical, and their size and shape suggested that they may correspond to a dimeric $CIII_2$ associated with a single CIV. Focused classification and processing of the subclass containing ~62,000 particles with the highest initial resolution, and best discernable features, led to a tripartite $CIII_2CIV$ map (SC-1A, EMD-22228) at 6.1Å resolution (**Fig. S3A**, see SI Methods for details), while another dataset yielded a slightly lower resolution map (SC-1B, EMD-22230) at 7.2Å (**Fig. S3B**) (**Table 1**). The larger particles (~250Å length, **Fig. S3**, Box 1) were more symmetrical and represented a dimeric $CIII_2$ flanked by two CIV (*i.e.*, $CIII_2CIV_2$), as expected based on two c_1-CcoP-c_y subunits *per* $CIII_2$. However these particles were rare (~5,000) and their map (SC-1C) could not be refined beyond ~10Å resolution (**Fig. S3C**).

The *R. capsulatus* cbb_3-type CIV is highly homologous to that of *P. stutzeri* but not identical (see Methods for details). Thus, a homology model of CIV was built using the *P. stutzeri* structure (PDB: 3MK7; 3.2Å resolution) as a template and validated (**Table S7**) (SI, Methods). In addition, the existing $CIII_2$ model (PDB: 1ZRT; 3.5Å resolution) was further refined (PDB: 6XI0; 3.3Å resolution) using our cryo-EM data (see below and **Table 2**). These models were fitted as rigid bodies into the maps SC1-A with a correlation coefficient CC_{box} of 0.75 and SC-1B with a correlation coefficient CC_{box} of 0.71 (**Fig. S4A**) (**Table 1**). The [2Fe-2S] clusters of the FeS proteins of $CIII_2$ could be recognized closer to heme b_L (b position) than to heme *c* (c position), but had lower occupancy and resolution likely due to conformational heterogeneity (**Fig. S4B**). In particular, the heterogeneity of the FeS-ED in monomer A (*i.e.*, adjacent to CIV) was more pronounced than that in monomer B (*i.e.*, away from CIV) of $CIII_2$. Lower resolutions of the FeS-ED portions were anticipated because of their

mobility (Darrouzet et al., 2001; Esser et al., 2006). Details of the tripartite $CIII_2CIV$ structure are described below together with the bipartite SC, which has a higher resolution.

Superimposition of the $CIII_2$ portions of SC-1A and SC-1B maps showed that CIV was in different orientations in different maps (**Fig. S4C**). The two extreme locations of CIV with respect to $CIII_2$ were displaced from each other by a translation of ~3Å and a rotation of ~37 degrees (**Fig. S4D, E**; SC-1A in red, and SC-1B in blue). Other subclasses identified in 3D classifications showed CIV in slightly different orientations between those seen in SC-1A and SC-2B maps. This variable rotation of CIV around $CIII_2$ is attributed to the limited interaction interface between the CcoP (N-ter TMH) of CIV and the cyt *b* (TMH7) of $CIII_2$ (see **Fig. 3C**), indicating that the $CIII_2CIV$ interface is flexible.

In the interface regions of SC-1A and SC-1B maps, additional weaker features that are not readily attributable to $CIII_2$ and CIV structures were also observed. Intriguingly though, no membrane-external features corresponding to cyt *c* domain of c_y, which is an integral part of the cyt c_1-CcoP-c_y subunit of tripartite $CIII_2CIV$, could be discerned in these maps.

Structure of bipartite SC supplemented with cyt c_y. In an attempt to locate the cyt *c* domain of c_y, the bipartite SC preparations devoid of it (**Fig. 2A**, fraction A-1) were supplemented with either purified full-length cyt c_y, or with its soluble variant lacking the TMH (*i.e.*, cyt S-c_y) (Ozturk et al., 2008), to yield the bipartite SC+c_y and SC+S-c_y samples. Following SEC, the elution fractions analyzed by SDS-PAGE showed that only the intact cyt c_y, but not the cyt S-c_y, associated with the SC (**Fig. S5A**). Thus, the cyt *c* domain of c_y does not bind tightly to, and its TMH is required for association with, this SC.

The cryo-EM analyses of the bipartite SC+c_y samples were carried out as above, and yielded a map (SC-2A, EMD-22227) at 5.2Å resolution (**Fig. S6A**,**B**), with local resolutions ranging from 4.3-8.0Å (**Fig. S7A**,**C**). The homology model of CIV and the refined model of $CIII_2$ (PDB: 6XI0) were

fitted as rigid bodies into SC-2A with a correlation coefficient CC_{box} of 0.74 (**Fig. 3A**) (**Table 1**). Comparison of SC-2A (bipartite $CIII_2CIV$) with SC-1A (tripartite $CIII_2CIV$) maps showed that they were highly similar with RMSD of 1.6 Å. They are collectively referred to as $CIII_2CIV$, irrespective of their bipartite or tripartite origins.

The dimensions of the slightly curved $CIII_2CIV$ structure (~155x60x90Å, LxWxH) were consistent with a $CIII_2$ dimer associated with one CIV. On SC-2A map at 5.2Å resolution, some large aromatic side chains could be discerned (**Fig. 3B**), and of the TMHs seen, 34 accounted for by two FeS proteins, two cyts *b* and two cyts c_1 (2, 16 and 2 TMHs per dimer, respectively) of $CIII_2$, and single CcoN, CcoO and CcoP (12, 1 and 1 TMHs, respectively) of CIV (**Fig. 3C**). The features corresponding to the heme cofactors of $CIII_2CIV$ were readily attributed to hemes b_H and b_L of cyt *b*, heme c_1 of cyt c_1, and to hemes *b* and b_3 of CcoN, heme *c* of CcoO and hemes c_{p1} and c_{p2} of CcoP proteins. As seen with the tripartite maps, the [2Fe-2S] clusters of $CIII_2$ could be recognized closer to heme b_L (in b position), but had lower resolution because of conformational heterogeneity.

An additional TMH was observed at the distal end of CIV (**Fig. 3A**, rotated 180 degrees in **Fig. 4A**) close to CcoN TMH3 and TMH4 (**Fig. 3C**). Due to its location, this TMH (depicted in **Fig. 3** and **Fig. 4** as an *ab initio* model of the CcoN Arg25-Leu48 residues generated by I-TASSER (Yang et al., 2015)) was tentatively attributed to the extra N-ter TMH (*i.e.*, TMH0) of CcoN (**Fig. 4B**).

The interface of $CIII_2CIV$ is roughly delimited by CcoN TMH8 and TMH9, CcoP TMH, cyt *b*-TMH5 and TMH7, and cyt c_1 C-ter TMH of monomer A, with the closest interaction being between CcoP TMH and cyt *b* TMH7 (**Fig. 3A,C**). Two highly confined inter-complex connections and two interacting TMHs of unknown identities were present at the interface (**Fig. 4A**, red and blue TMHs). One such connection was at the *n* face of the membrane, near the cyt c_1 and CcoP TMHs (**Fig. 4C**, $Lys257_{c1}$ and $Thr13_{CcoP}$). These subunits being covalently linked, the connecting feature in the map was tentatively attributed to their junction linking $CIII_2$ and CIV.

The assembly factor CcoH and cyt c_y TMHs are located at $CIII_2CIV$ interface. The identities of the unknown TMHs at the interface of $CIII_2CIV$ (**Fig. 3** and **Fig. 4)** were sought using a co-evolution based approach, RaptorX-ComplexContact (Zeng et al., 2018), predicting the residue-residue contacts in protein-protein interactions. All known single TMH containing CIV-related proteins (*i.e.*, CcoQ subunit, CcoS and CcoH assembly factors (Koch et al., 2000) and cyt c_y (Myllykallio et al., 1997)) were analyzed against all subunits of $CIII_2$ and CIV. Significant predictions of interacting residue pairs (confidence value >0.5) were observed only between CcoN (primarily TMH9) and the putative CcoH N-term TMH (**Table S4**). An *ab initio* model of CcoH TMH (**Fig. S8A**, residues 11 to 35) was generated by I-TASSER (Yang and Zhang, 2015), and docked onto CIV using PatchDock (Schneidman-Duhovny et al., 2005) with the predicted residue-residue contacts as distance restraints (15 Å threshold) and without using the corresponding cryo-EM maps (SI, Methods). The top scoring models converged to a single cluster around the location of the unknown TMH, close to CcoN TMH9 at $CIII_2CIV$ interface (**Fig. S8B**). Close examination of the interactions between CcoH TMH and CcoN TMH9 showed that multiple co-evolutionarily conserved residues are in close contacts (**Fig. S8C**). Earlier studies had suggested that CcoH is near the CcoP and CcoN, to which it can be cross-linked by disuccinimidyl suberate (DSS, spacer length ~11Å) (Pawlik et al., 2010). Thus, the unknown TMH located close to CcoN TMH9 (**Fig. 3C** and **Fig. 4C**, blue TMH) was tentatively assigned to the assembly factor CcoH.

An important difference between the maps of the bipartite $CIII_2CIV+c_y$ (SC-2A) and tripartite $CIII_2CIV$ (SC-1A) was in the features corresponding to the unidentified TMHs at the interface. These densities were barely visible in SC-1A, but highly enhanced in SC-2A (**Fig. 4C**), indicating higher occupancy. The observation that only the native cyt c_y binds to bipartite SC via its TMH (not its cyt *c* domain, *i.e.*, cyt S-c_y), suggested that the TMH (red in **Fig. 4C)**, next to CcoH TMH (blue in **Fig.**

4C), may correspond to the membrane-anchor of cyt c_y. This explanation is most plausible since the bipartite $CIII_2CIV+c_y$ samples were supplemented with full-length cyt c_y while the tripartite samples contained only the fused cyt *c* domain but not the TMH. Indeed, landmark densities corresponding to the helix-breaking Gly11 and two correctly spaced bulky sides chains of Phe15 and Tyr21 of cyt c_y TMH (NH_2-xxx**Gly11**xxx**Phe15**xxxxx**Tyr21**-COOH) were discerned (**Fig. 4D**).

Additionally, some $CIII_2CIV+c_y$ subclasses exhibited a weak feature on the *p* side of the membrane that may reflect the cyt *c* domain of c_y (**Fig. S6G,** SC-2B). However, this feature could not be refined to high resolution, consistent with the weak binding of cyt *c* domain of c_y to $CIII_2CIV$ (**Fig. S5A**). Moreover, the predominant conformation of CIV in the bipartite $CIII_2CIV+c_y$ (**Fig. S6A**,**B**, SC-2A) shifted towards that found in SC-1A map of tripartite SC (**Fig. S3A**), with no major class corresponding to SC-1B. This suggested that the local interactions between the CcoH and cyt c_y TMHs and CIV decreased the interface flexibility of $CIII_2CIV$ (**Fig. 4C**).

Cryo-EM structures of *R. capsulatus* native $CIII_2$. During this study we noted that the bipartite $SC+c_y$ samples contained large amounts of smaller particles (~110Å length, **Fig. S3**, Box 2) that were the size of $CIII_2$ (**Fig. S6C,D).** Analyses of these particles using C2 symmetry led to the map $CIII_2$ at 3.3Å resolution for native $CIII_2$ (**Fig. S6E**), with local resolutions ranging from 3.0 to 4.0Å (**Fig. S7B**,**D**) (**Table 2**). The FeS-ED parts showed a lower occupancy and resolution compared to the rest of the map, indicating conformational heterogeneity. Interestingly, when similar analyses were carried out without imposing C2 symmetry, three distinct maps ($CIII_2$ c-c, $CIII_2$ b-c and $CIII_2$ b-b) for $CIII_2$ were obtained at 3.8, 4.2 and 3.5Å resolutions, respectively (**Fig. S6F**). These maps were superimposable with respect to cyt *b* and cyt c_1 subunits, except for the FeS-ED portions. The $CIII_2$ structures depicted by the $CIII_2$ b-b (**Fig. 5A-C**) and $CIII_2$ c-c (**Fig. 5D**) maps exhibited overall C2 symmetry, but in the former the FeS-EDs were located in b, whereas in the latter they were in c

position (Esser et al., 2006). Notably, the third structure (**Fig. S6F**, $CIII_2$ b-c*)* was asymmetric, with the FeS-ED of one monomer being in c, and the other in b positions (**Fig. 5E**). Such asymmetric structures of native $CIII_2$ have been rarely seen using crystallographic approaches, although proposed to occur during QH_2 oxidation by $CIII_2$ (Castellani et al., 2010; Cooley et al., 2009; Covian and Trumpower, 2005). Similar low occupancy and resolution of the FeS-EDs, suggesting conformational heterogeneity, were also seen with the $CIII_2CIV$ maps.

Interactions of cyt c_2 and cyt c_y with $CIII_2CIV$. The interaction interfaces between $CIII_2CIV$ and its physiological electron carriers were pursued using cross-linking mass spectrometry (XL-MS) (Gotze et al., 2015; Slavin and Kalisman, 2018). First, the co-crystal structure (PDB: 3CX5) of yeast $CIII_2$ with its soluble electron carrier iso-1 cyt *c* (Solmaz and Hunte, 2008) was used as a template (homology between yeast cyt c_1 and *R. capsulatus* cyt c_1: 31% identity and 58% similarity; iso-cyt *c* and cyt c_2: 25% identity and 56% similarity) to model the binding of cyt c_2 on bacterial $CIII_2$. As the co-crystal structure contains only one iso-1 cyt *c* bound to one of the two cyt c_1 of yeast $CIII_2$, *R. capsulatus* cyt c_1 (PDB: 6XI0) and cyt c_2 (PDB: 1C2N) structures were superimposed with their counterparts on the co-crystal structure, and a model with a single cyt c_2 docked to one monomer of $CIII_2$ was generated. To experimentally verify this model, the protein cross-linker 4-(4,6-dimethoxy-1,3,5-triazin-2-yl)-4-methyl-morpholinium chloride (DMTMM) was used with *R. capsulatus* cyt c_2 bound to $CIII_2$ (SI, Methods). Multiple intra-subunit cross-links (XLs) within $CIII_2CIV$ detected in several experiments served as controls (**Table S5** and **Fig. S9A)**. High-confidence XLs were obtained using both FindXL (Kalisman et al., 2012) and MeroX (Iacobucci et al., 2018) search engines, and only those identified by both were retained. The three XLs between cyt c_1 and cyt c_2 provided distance restraints (~30Å for DMTMM) for docking cyt c_2 to $CIII_2$ using PatchDock (**Table S5** and **Fig. S9B**). The docking models clustered at a single region per monomer of $CIII_2$ (**Fig. 6A**, right), which

overlapped with the binding site of cyt c_2 defined by the model generated by alignment to the yeast co-crystal structure (**Fig. S9C**). The distance from cyt c_2 heme-Fe to cyt c_1 heme-Fe is ~16.8Å for the co-crystal derived model, while comparable distances between ~13.8 - 20.4Å were obtained with the docking models. Thus, docking with Patchdock integrating XL-MS based distance restraints defined reliably, but with limited accuracy, the interaction region of cyt c_2 on $CIII_2$.

No information about the binding sites between cyt c_2 and cbb_3-type CIV was available, so the XL-MS with DMTMM was extended to this case. Similarly, the XLs found between the proteins (1 between cyt c_2 and CcoP, and 8 between cyt c_2 and CcoO) provided distance restraints for docking cyt c_2 to CIV via Patchdock (**Table S5**). The cyt c_2 docking models also clustered in a single region of CIV (**Fig. 6A**, left), closer to heme c_{p2} (c_2 heme-Fe to c_{p2} heme-Fe: ~15.2 to 35.6Å) than heme c_{p1} (c_2 heme-Fe to c_{p1} heme-Fe: ~23.0 to 42.0Å) of CcoP subunit (**Fig. 7**). Surface charge complementarities between the positively charged face of cyt c_2 and the negatively charged likely binding regions on both CIV and on $CIII_2$ are seen (**Fig. S10A**). These two cyt c_2 binding regions on $CIII_2CIV$ are distant from each other (closest c_2 heme-Fe on $CIII_2$ to that on CIV is ~69Å) (**Fig. 7A**).

Next, the binding interactions between cyt *c* domain of c_y and $CIII_2CIV$ were addressed using DMTMM and disuccinimidyl dibutyric urea (DSBU) as cross-linkers. Similar to DMTMM, DSBU yielded multiple intra-subunit XLs within the subunits of $CIII_2CIV$, providing experimental controls (**Table S6** and **Fig. S9D**). Six XLs (five cyt c_y to cyt c_1 and one cyt c_y to FeS protein) with DMTMM (**Table S5**) and four XLs (only cyt c_y to FeS protein) with DSBU (**Table S6**) were identified. Although chemically different cross-linkers were used, XLs were observed only between cyt c_y and $CIII_2$, and not with CIV, suggesting that this cyt *c* domain is closer to $CIII_2$ in $CIII_2CIV$. Using the XLs as distance restraints (~35Å for DSBU and ~30Å for DMTMM) PatchDock generated two binding clusters for cyt *c* domain of c_y on each $CIII_2$ monomer of SC. One of the clusters was on cyt c_1, overlapping with the binding region of cyt c_2 (**Fig. 6B**), whereas the other one was located between

cyt c_1 and the FeS-ED near the inter-monomer region of $CIII_2$ (**Fig. S11**). To further support these binding locations obtained by XL-MS-based docking, we sought classes that have extra densities corresponding to cyt *c* domain of c_y in our cryo-EM datasets, and found a minor 3D class containing ~18,000 particles (**Fig. S6G**), which has an extra feature between CIV and CIII that may be attributable to this domain (**Fig. S11**). The two docking clusters, clearly visible in top view (**Fig. S11C**), were more spread out compared with those of cyt c_2 (**Fig. 6A**, **Fig. 7A,C**), with the distances between cyt c_y heme-Fe and cyt c_1 heme-Fe of $CIII_2$ monomer A being between 13.8 to 47.1Å, consistent with the weak binding of cyt *c* domain of c_y.

Patchdock mediated docking of cyt *c* domain of c_y was also performed with the same XLs as above but using the conformers of native $CIII_2$ with differently located FeS-EDs (**Fig. 5C-E**, $CIII_2$ b-b, c-c and b-c). The data showed that when the FeS-EDs are in c position ($CIII_2$ c-c), the docking models gathered as a single cluster on cyt c_1, slightly displaced towards the FeS-ED of the same monomer (**Fig. S12A-C**). However, when the FeS-EDs are in b position ($CIII_2$ b-b), such models were more spread out (**Fig. S12D-F**). The third model with one FeS-ED in c and the other in b positions showed the expected clustering pattern depending on the local FeS-ED conformation. As in the SC both FeS-EDs appear to be in the b position, we assume that the docking pattern of cyt *c* domain of c_y is like that seen with $CIII_2$ b-b. Thus, the relatively spread docking position observed with SC (**Fig. 7**, **Fig. S11**) was attributed to variable conformations of the FeS-EDs on $CIII_2$. Furthermore, since heme c_1, and not the FeS protein, is the electron exit site of $CIII_2$ (Crofts et al., 2008; Osyczka et al., 2005), the cluster on cyt c_1 was taken as the productive binding region of cyt *c* domain of c_y.

Examination of all pertinent distances between the cofactors of $CIII_2CIV$ (**Fig. 7A**) indicates that the binding region of cyt *c* domain of c_y near heme c_1 of $CIII_2$ is far away from the expected electron entry point(s) of CIV. The large distance (~50.8Å) separating cyt c_1 heme-Fe of $CIII_2$ monomer A from CcoP c_{p1} heme-Fe (the closest compared with heme c_{p2} of CIV) renders it impossible to define a

location for cyt c_y close enough to heme c_1 reducing it, and heme c_{p1} oxidizing it, to sustain productive electron transfer from $CIII_2$ to CIV. This distance constraint, the inability to resolve the cyt *c* domain of cyt c_y by cryo-EM, and the higher frequency of XLs to $CIII_2$ strongly infer that the cyt *c* domain of c_y must oscillate to carry out soluble carrier-independent electron transfer within $CIII_2CIV$ to couple QH_2 oxidation to O_2 reduction (**Fig. 8**).

Discussion

Prior to this work, no structural information was available on any bacterial *cbb*$_3$-type CIV containing SC, or on its interactions with its physiological redox partners. Here, we describe the first cryo-EM structures of CIII$_2$CIV, a *bc*$_1$-*cbb*$_3$ type respiratory SC from the Gram-negative, facultative phototroph *R. capsulatus*. We also define the likely binding regions of the electron carriers cyt c_2 and cyt c_y to CIII$_2$CIV, and report the structures of both homo- and hetero-dimeric conformers of native CIII$_2$. Although X-ray based structures of bacterial *bc*$_1$-type CIII$_2$ are available, native CIII$_2$ heterodimers have not been observed frequently. Similarly, only a single structure, that of *P. stutzeri* (Buschmann et al., 2010), was available for *cbb*$_3$-type CIV. Members of this subfamily of heme-Cu:O_2 reductases are widespread among bacteria and essential for major micro-aerobic processes, including anaerobic photosynthesis, nitrogen fixation, symbiosis and bacterial infection (Khalfaoui-Hassani et al., 2016). Unlike the obligate CIII$_2$CIV$_2$ SC of *Actinobacteria*, which is rigid and devoid of a free electron carrier (Gong et al., 2018; Wiseman et al., 2018), the *R. capsulatus* facultative CIII$_2$CIV is naturally of low abundance and flexible, limiting its structural resolution. The dual function of bacterial CIII$_2$ interacting with both the photochemical reaction center in photosynthesis, and cyt *c* oxidase in respiration, may necessitate this natural plasticity to allow swift metabolic adaptations. Similar flexibilities have also been seen with the yeast and human SCs (Sousa and Vonck, 2019).

Isolation of CIII$_2$CIV was only possible using a genetically modified strain carrying a translational fusion between CIII$_2$ and CIV (SI, Methods). Despite the complexity of translocation, maturation and assembly processes of multi-cofactor containing membrane complexes, this fusion approach is of general use. Our fused SC preparations were compositionally heterogeneous, containing mixtures of CIII$_2$CIV$_2$, CIII$_2$CIV and CIII$_2$ particles. The basis of this heterogeneity is unclear, though it may stem from subunit sub-stoichiometry, incomplete assembly, or higher susceptibility to degradation during sample preparations. Insertion of different spacers at the cyt c_1-CcoP fusion junction, overexpression

of the subunits and the related assembly components could not overcome the heterogeneity (SI, Methods). Consequently, structural studies required extensive data collections and limited structural resolutions, but allowed analyses of fragmented particles.

Structures of $CIII_2CIV$. The structures of the tripartite $CIII_2CIV$ or bipartite $CIII_2CIV+c_y$ at sub-nanometer resolution (~5.2 to 7.2Å) were highly similar. Limited protein-protein interaction between the subunits of $CIII_2$ and CIV was seen at the interface where the TMHs of cyt c_y and CcoH were located (**Fig. 4**), limiting the flexibility of $CIII_2CIV$. Another helix-like feature found at the exterior edge of CIV was attributed to the extra N-ter helix (TMH0) unique to *R. capsulatus* CcoN. However, due to the limited resolutions of the structures, these attributions are tentative. Limited resolution also precluded identification of non-protein constituents at the $CIII_2CIV$ interface. In this respect, *R. capsulatus* lacks cardiolipin, often implicated in SC stability (Arias-Cartin et al., 2012). Instead, it produces ornithine lipid that can mimic cardiolipin upon dimerization (Aygun-Sunar et al., 2006). Ornithine lipid-less mutants contain very low amounts of CIV and $CIII_2$, and if any SC is unknown.

Previously, neither the exact location nor the mobility of cyt c_y, which is the basis of the "soluble carrier-independent" electron transfer from $CIII_2$ to CIV, were known. The SC structure shows that locking the N-terminal TMH of cyt c_y at the interface allows mobility of its cyt *c* domain (**Fig. 8**). The linker region attaching the TMH to cyt *c* domain remains unresolved, but is long enough to allow oscillations between $CIII_2$ and CIV. Earlier studies with *R. capsulatus* cyt c_y had shown that a full-length linker is needed for rapid (< ~50 μsec) electron transfer from $CIII_2$ to the photosynthetic reaction center in photosynthesis (Myllykallio et al., 1998). In contrast, a shorter linker (~45-residue instead of 69) is fully proficient for respiratory electron transfer to CIV (Daldal et al., 2001).

Structures of bacterial native $CIII_2$. In native $CIII_2$ conformers, different positions of the [2Fe-2S] cluster bearing FeS-EDs were seen. Crystallographic structures have often depicted bacterial $CIII_2$ as symmetrical homodimers (Berry et al., 2004; Esser et al., 2006; Xia et al., 2008). These structures

were obtained in the presence of inhibitors constraining FeS-EDs near heme b_L or used mutants stabilizing it on cyt *b* surface. Alternatively, they contained crystal contacts restricting the FeS-ED movement (Esser et al., 2008). To our knowledge, no native heterodimeric $CIII_2$ structure of bacterial origin with different conformations of its FeS-EDs has been reported. Only recently, the cryo-EM structures of mitochondrial SCs with different maps for $CIII_2$ FeS-EDs have been reported (Letts et al., 2019; Sousa et al., 2016). Thus, native $CIII_2$ is not always a symmetric homodimer, and the FeS-ED of each monomer is free to move independently from each other, which has functional implications. The Q-cycle models describe the mechanism of $CIII_2$ catalysis by two turnovers of a given monomer (Crofts and Berry, 1998; Crofts et al., 2008; Osyczka et al., 2005). The mobility of the FeS-ED between the b and c positions is essential for QH_2 oxidation, and the different positions of the FeS-ED protein are often attributed to different catalytic steps (Esser et al., 2006). Emerging asymmetric structures of bacterial and mitochondrial native $CIII_2$ obtained by cryo-EM in the absence of inhibitors or mutations, combined with the well-established inter-monomer electron transfer between the heme b_L of the monomers (Lanciano et al., 2013; Lanciano et al., 2011; Swierczek et al., 2010; Yu et al., 2002), start to provide a glimpse into plausible "heterodimeric Q cycle" mechanism(s) (Castellani et al., 2010; Cooley, 2010; Cooley et al., 2009), at least when $CIII_2$ is a part of SCs. Accordingly, $CIII_2$ may cycle between homo- and hetero-dimeric conformations in regards to its FeS-EDs during catalysis. These mechanistic implications remain to be studied.

Electronic communication between $CIII_2CIV$ partners. Earlier, binding interactions between $CIII_2CIV$ and its physiological electron carriers were unknown. Here we defined the likely interaction regions between the cyt c_2 or the cyt c_y and $CIII_2CIV$ (**Fig. 8**). The $CIII_2CIV$ structure indicates that the distances separating heme c_1 of $CIII_2$ monomer **A** and hemes c_{p1} and c_{p2} of CIV are too large (**Fig. 7**) for direct microsecond scale electronic communication (Moser et al., 1992) to sustain the turnover

rate of $CIII_2CIV$. Thus, even when $CIII_2$ and CIV form a SC, a freely diffusing cyt c_2 or a membrane-anchored mobile cyt c_y, is required for QH_2:O_2 oxidation.

The binding region of cyt c_2 on $CIII_2$ was identified earlier (Solmaz and Hunte, 2008), but that on CIV was unknown. The binding location of cyt c_2 on CIV determined in this study, the redox midpoint potentials (E_m) of the cofactors and the distances separating them (**Fig. 7A**) suggest that cyt c_2 would confer electrons to the closer heme c_{p2}, rather than the more distant heme c_{p1}, of CcoP. This will then initiate canonical electron transfer via heme c_{p1}, heme c_o and heme b to heme b_3-Cu_B site for O_2 reduction (Brzezinski and Gennis, 2008; Wikstrom et al., 2018) (**Fig. 8**). For purified *R. capsulatus* proteins, the E_m value of cyt c_2 is ~350 mV (Myllykallio et al., 1999), while those of $CIII_2$ heme c_1 and CIV heme c_o are ~320 mV (Valkova-Valchanova et al., 1998) and ~210 mV (Gray et al., 1994), respectively. The E_m values of *R. capsulatus* CIV hemes c_{p1} and c_{p2} are unknown, but based on similar E_m values of heme c_o for *B. japonicum* (200 mV) and *R. capsulatus* (210 mV), they are expected to be close to those of *B. japonicum* c_{p1} (~300 mV) and c_{p2} (~390 mV) (Verissimo et al., 2007).

In the case of cyt c_y, its interaction region on CIV remains less well defined. Of the two binding regions of cyt c_y on $CIII_2$, that on cyt c_1 was taken as the most likely functional site. This binding region on cyt c_1 is close to that of cyt c_2, but cyt c_y has less complementary surface charges (**Fig. S10B**), consistent with its weaker binding to $CIII_2CIV$. Anchoring cyt c_y to the membrane, next to its redox partners, might have enhanced its electron transfer efficiency while minimizing its electrostatic interactions with its partners.

The distance separating the redox centers is a major factor that controls the rate of electron transfer (Moser et al., 1992). The binding region of cyt c domain of c_y on $CIII_2$ suggests that reduced cyt c_y, upon its movement to CIV, might preferentially convey electrons to the closer heme c_{p1} than heme c_{p2} of CcoP (**Fig. 8**). If so, then under physiological conditions, heme c_{p1} would be the primary receiver of electrons derived from QH_2 oxidation by $CIII_2$, forming a fully membrane-confined electronic

wiring within $CIII_2CIV$. In contrast, cyt c_2 carries electrons from heme c_1 to heme c_{p2} via free diffusion. Significantly, this membrane-external pathway might accommodate electrons not only from QH_2 but also from other donors distinct from $CIII_2$. As such, reduction of cyt c_2 during methylamine oxidation (Otten et al., 2001), or degradation of sulfur containing amino acids, converting toxic sulfite (SO_3^{2-}) to sulfate (SO_4^{-2}) by sulfate oxidase (Kappler and Dahl, 2001) might provide electrons to CIV, contributing to cellular energy production.

In summary, for the first time, the architecture of $CIII_2CIV$ SC along with its dynamics and interactions with its physiological redox partners established salient structural features of two distinct respiratory electron transport pathways (membrane-confined and membrane-external) that operate between $CIII_2$ and CIV in Gram-negative bacteria.

References

Acin-Perez, R., and Enriquez, J.A. (2014). The function of the respiratory supercomplexes: the plasticity model. Biochim Biophys Acta *1837*, 444-450.

Albert, I., Rutherford, A.W., Grav, H., Kellermann, J., and Michel, H. (1998). The 18 kDa cytochrome c_{553} from *Heliobacterium gestii*: gene sequence and characterization of the mature protein. Biochemistry *37*, 9001-9008.

Arias-Cartin, R., Grimaldi, S., Arnoux, P., Guigliarelli, B., and Magalon, A. (2012). Cardiolipin binding in bacterial respiratory complexes: structural and functional implications. Biochim Biophys Acta *1817*, 1937-1949.

Aspholm, M., Aas, F.E., Harrison, O.B., Quinn, D., Vik, A., Viburiene, R., Tonjum, T., Moir, J., Maiden, M.C., and Koomey, M. (2010). Structural alterations in a component of cytochrome *c* oxidase and molecular evolution of pathogenic *Neisseria* in humans. PLoS Pathog *6*, e1001055.

Aygun-Sunar, S., Mandaci, S., Koch, H.G., Murray, I.V., Goldfine, H., and Daldal, F. (2006). Ornithine lipid is required for optimal steady-state amounts of *c*-type cytochromes in *Rhodobacter capsulatus*. Mol Microbiol *61*, 418-435.

Bergdoll, L., Brink, F., Nitschke, W., Picot, D., and Baymann, F. (2016). From low- to high-potential bioenergetic chains: Thermodynamic constraints of Q-cycle function. Biochim Biophys Acta *1857*, 1569-1579.

Berry, E.A., Huang, L.S., Saechao, L.K., Pon, N.G., Valkova-Valchanova, M., and Daldal, F. (2004). X-Ray Structure of *Rhodobacter capsulatus* Cytochrome bc_1: Comparison with its Mitochondrial and Chloroplast Counterparts. Photosynth Res *81*, 251-275.

Berry, E.A., and Trumpower, B.L. (1985). Isolation of ubiquinol oxidase from *Paracoccus denitrificans* and resolution into cytochrome bc_1 and cytochrome c-aa_3 complexes. J Biol Chem *260*, 2458-2467.

Bott, M., Ritz, D., and Hennecke, H. (1991). The *Bradyrhizobium japonicum cycM* gene encodes a membrane-anchored homolog of mitochondrial cytochrome *c*. J Bacteriol *173*, 6766-6772.

Brzezinski, P. (2019). New Structures Reveal Interaction Dynamics in Respiratory Supercomplexes. Trends Biochem Sci.

Brzezinski, P., and Gennis, R.B. (2008). Cytochrome *c* oxidase: exciting progress and remaining mysteries. J Bioenerg Biomembr *40*, 521-531.

Buschmann, S., Warkentin, E., Xie, H., Langer, J.D., Ermler, U., and Michel, H. (2010). The structure of cbb_3 cytochrome oxidase provides insights into proton pumping. Science *329*, 327-330.

Castellani, M., Covian, R., Kleinschroth, T., Anderka, O., Ludwig, B., and Trumpower, B.L. (2010). Direct demonstration of half-of-the-sites reactivity in the dimeric cytochrome bc1 complex: enzyme with one inactive monomer is fully active but unable to activate the second ubiquinol oxidation site in response to ligand binding at the ubiquinone reduction site. J Biol Chem *285*, 502-510.

Cooley, J.W. (2010). A structural model for across membrane coupling between the Q_o and Q_i active sites of cytochrome bc_1. Biochim Biophys Acta *1797*, 1842-1848.

Cooley, J.W., Lee, D.W., and Daldal, F. (2009). Across membrane communication between the Q_o and Q_i active sites of cytochrome bc_1. Biochemistry *48*, 1888-1899.

Covian, R., and Trumpower, B.L. (2005). Rapid electron transfer between monomers when the cytochrome bc_1 complex dimer is reduced through center N. J Biol Chem *280*, 22732-22740.

Crofts, A.R., and Berry, E.A. (1998). Structure and function of the cytochrome bc_1 complex of mitochondria and photosynthetic bacteria. Curr Opin Struct Biol *8*, 501-509.

Crofts, A.R., Holland, J.T., Victoria, D., Kolling, D.R., Dikanov, S.A., Gilbreth, R., Lhee, S., Kuras, R., and Kuras, M.G. (2008). The Q-cycle reviewed: How well does a monomeric mechanism of the bc(1) complex account for the function of a dimeric complex? Biochim Biophys Acta *1777*, 1001-1019.

Daldal, F., Cheng, S., Applebaum, J., Davidson, E., and Prince, R.C. (1986). Cytochrome c_2 is not essential for photosynthetic growth of *Rhodopseudomonas capsulata*. Proc Natl Acad Sci U S A *83*, 2012-2016.

Daldal, F., Mandaci, S., Winterstein, C., Myllykallio, H., Duyck, K., and Zannoni, D. (2001). Mobile cytochrome c_2 and membrane-anchored cytochrome c_y are both efficient electron donors to the cbb_3- and aa_3-type cytochrome *c* oxidases during respiratory growth of *Rhodobacter sphaeroides*. J Bacteriol *183*, 2013-2024.

Darrouzet, E., Moser, C.C., Dutton, P.L., and Daldal, F. (2001). Large scale domain movement in cytochrome bc_1: a new device for electron transfer in proteins. Trends Biochem Sci *26*, 445-451.

Davidson, E., Ohnishi, T., Tokito, M., and Daldal, F. (1992). *Rhodobacter capsulatus* mutants lacking the Rieske FeS protein form a stable cytochrome bc_1 subcomplex with an intact quinone reduction site. Biochemistry *31*, 3351-3358.

Ducluzeau, A.L., Ouchane, S., and Nitschke, W. (2008). The cbb_3 oxidases are an ancient innovation of the domain bacteria. Mol Biol Evol *25*, 1158-1166.

Enriquez, J.A. (2016). Supramolecular Organization of Respiratory Complexes. Annu Rev Physiol *78*, 533-561.

Esser, L., Elberry, M., Zhou, F., Yu, C.A., Yu, L., and Xia, D. (2008). Inhibitor-complexed structures of the cytochrome bc_1 from the photosynthetic bacterium *Rhodobacter sphaeroides*. J Biol Chem *283*, 2846-2857.

Esser, L., Gong, X., Yang, S., Yu, L., Yu, C.A., and Xia, D. (2006). Surface-modulated motion switch: capture and release of iron-sulfur protein in the cytochrome bc_1 complex. Proc Natl Acad Sci U S A *103*, 13045-13050.

Gong, H., Li, J., Xu, A., Tang, Y., Ji, W., Gao, R., Wang, S., Yu, L., Tian, C., Li, J., *et al.* (2018). An electron transfer path connects subunits of a mycobacterial respiratory supercomplex. Science *362*.

Gotze, M., Pettelkau, J., Fritzsche, R., Ihling, C.H., Schafer, M., and Sinz, A. (2015). Automated assignment of MS/MS cleavable cross-links in protein 3D-structure analysis. J Am Soc Mass Spectrom *26*, 83-97.

Gray, K.A., Grooms, M., Myllykallio, H., Moomaw, C., Slaughter, C., and Daldal, F. (1994). *Rhodobacter capsulatus* contains a novel *cb*-type cytochrome *c* oxidase without a Cu_A center. Biochemistry *33*, 3120-3127.

Gu, J., Wu, M., Guo, R., Yan, K., Lei, J., Gao, N., and Yang, M. (2016). The architecture of the mammalian respirasome. Nature *537*, 639-643.

Hartley, A.M., Lukoyanova, N., Zhang, Y., Cabrera-Orefice, A., Arnold, S., Meunier, B., Pinotsis, N., and Marechal, A. (2019). Structure of yeast cytochrome *c* oxidase in a supercomplex with cytochrome bc_1. Nat Struct Mol Biol *26*, 78-83.

Hochkoeppler, A., Jenney, F.E., Jr., Lang, S.E., Zannoni, D., and Daldal, F. (1995). Membrane-associated cytochrome c_y of *Rhodobacter capsulatus* is an electron carrier from the cytochrome bc_1 complex to the cytochrome *c* oxidase during respiration. J Bacteriol *177*, 608-613.

Iacobucci, C., Gotze, M., Ihling, C.H., Piotrowski, C., Arlt, C., Schafer, M., Hage, C., Schmidt, R., and Sinz, A. (2018). A cross-linking/mass spectrometry workflow based on MS-cleavable cross-linkers and the MeroX software for studying protein structures and protein-protein interactions. Nat Protoc *13*, 2864-2889.

Jenney, F.E., Jr., and Daldal, F. (1993). A novel membrane-associated *c*-type cytochrome, cyt c_y, can mediate the photosynthetic growth of *Rhodobacter capsulatus* and *Rhodobacter sphaeroides*. EMBO J *12*, 1283-1292.

Kalisman, N., Adams, C.M., and Levitt, M. (2012). Subunit order of eukaryotic TRiC/CCT chaperonin by cross-linking, mass spectrometry, and combinatorial homology modeling. Proc Natl Acad Sci U S A *109*, 2884-2889.

Kao, W.C., Kleinschroth, T., Nitschke, W., Baymann, F., Neehaul, Y., Hellwig, P., Richers, S., Vonck, J., Bott, M., and Hunte, C. (2016). The obligate respiratory supercomplex from *Actinobacteria*. Biochim Biophys Acta *1857*, 1705-1714.

Kappler, U., and Dahl, C. (2001). Enzymology and molecular biology of prokaryotic sulfite oxidation. FEMS Microbiol Lett *203*, 1-9.

Khalfaoui-Hassani, B., Verissimo, A.F., Shroff, N., Ekici, S., Trasnea, P.-I., Utz, M., Koch, H.-G., and Daldal, F. (2016). Biogenesis of cytochrome *c* complexes: from insertion of redox cofactors to assembly of different subunits. In Cytochrome Complexes: Evolution, Structures, Energy Transduction, and Signaling, W. Cramer, and T. Kallas, eds. (Dordrecht: Springer), pp. 527-555.

Kim, M.S., Jang, J., Ab Rahman, N.B., Pethe, K., Berry, E.A., and Huang, L.S. (2015). Isolation and Characterization of a Hybrid Respiratory Supercomplex Consisting of *Mycobacterium tuberculosis* Cytochrome *bcc* and *Mycobacterium smegmatis* Cytochrome aa_3. J Biol Chem *290*, 14350-14360.

Koch, H.G., Winterstein, C., Saribas, A.S., Alben, J.O., and Daldal, F. (2000). Roles of the *ccoGHIS* gene products in the biogenesis of the cbb_3-type cytochrome *c* oxidase. J Mol Biol *297*, 49-65.

Kulajta, C., Thumfart, J.O., Haid, S., Daldal, F., and Koch, H.G. (2006). Multi-step assembly pathway of the cbb_3-type cytochrome *c* oxidase complex. J Mol Biol *355*, 989-1004.

Lanciano, P., Khalfaoui-Hassani, B., Selamoglu, N., and Daldal, F. (2013). Intermonomer electron transfer between the *b* hemes of heterodimeric cytochrome bc_1. Biochemistry *52*, 7196-7206.

Lanciano, P., Lee, D.W., Yang, H., Darrouzet, E., and Daldal, F. (2011). Intermonomer electron transfer between the low-potential *b* hemes of cytochrome bc_1. Biochemistry *50*, 1651-1663.

Lee, D.W., Ozturk, Y., Osyczka, A., Cooley, J.W., and Daldal, F. (2008). Cytochrome bc_1-c_y fusion complexes reveal the distance constraints for functional electron transfer between photosynthesis components. J Biol Chem *283*, 13973-13982.

Letts, J.A., Fiedorczuk, K., Degliesposti, G., Skehel, M., and Sazanov, L.A. (2019). Structures of Respiratory Supercomplex I+III2 Reveal Functional and Conformational Crosstalk. Mol Cell *75*, 1131-1146 e1136.

Letts, J.A., Fiedorczuk, K., and Sazanov, L.A. (2016). The architecture of respiratory supercomplexes. Nature *537*, 644-648.

Letts, J.A., and Sazanov, L.A. (2017). Clarifying the supercomplex: the higher-order organization of the mitochondrial electron transport chain. Nat Struct Mol Biol *24*, 800-808.

Melo, A.M., and Teixeira, M. (2016). Supramolecular organization of bacterial aerobic respiratory chains: From cells and back. Biochim Biophys Acta *1857*, 190-197.

Milenkovic, D., Blaza, J.N., Larsson, N.G., and Hirst, J. (2017). The Enigma of the Respiratory Chain Supercomplex. Cell Metab *25*, 765-776.

Moser, C.C., Keske, J.M., Warncke, K., Farid, R.S., and Dutton, P.L. (1992). Nature of biological electron transfer. Nature *355*, 796-802.

Myllykallio, H., Drepper, F., Mathis, P., and Daldal, F. (1998). Membrane-anchored cytochrome c_y mediated microsecond time range electron transfer from the cytochrome bc_1 complex to the reaction center in *Rhodobacter capsulatus*. Biochemistry *37*, 5501-5510.

Myllykallio, H., Drepper, F., Mathis, P., and Daldal, F. (2000). Electron-transfer supercomplexes in photosynthesis and respiration. Trends Microbiol *8*, 493-494.

Myllykallio, H., Jenney, F.E., Jr., Moomaw, C.R., Slaughter, C.A., and Daldal, F. (1997). Cytochrome c_y of *Rhodobacter capsulatus* is attached to the cytoplasmic membrane by an uncleaved signal sequence-like anchor. J Bacteriol *179*, 2623-2631.

Myllykallio, H., Zannoni, D., and Daldal, F. (1999). The membrane-attached electron carrier cytochrome c_y from *Rhodobacter sphaeroides* is functional in respiratory but not in photosynthetic electron transfer. Proc Natl Acad Sci U S A *96*, 4348-4353.

Nicholls, D.G., and Ferguson, S.J. (2013). Bioenergetics 4 (Elsevier).

Niebisch, A., and Bott, M. (2003). Purification of a cytochrome *bc-aa*$_3$ supercomplex with quinol oxidase activity from *Corynebacterium glutamicum*. Identification of a fourth subunity of cytochrome *aa*$_3$ oxidase and mutational analysis of diheme cytochrome c_1. J Biol Chem *278*, 4339-4346.

Osyczka, A., Moser, C.C., and Dutton, P.L. (2005). Fixing the Q cycle. Trends Biochem Sci *30*, 176-182.

Otten, M.F., van der Oost, J., Reijnders, W.N., Westerhoff, H.V., Ludwig, B., and Van Spanning, R.J. (2001). Cytochromes c_{550}, c_{552}, and c_1 in the electron transport network of *Paracoccus denitrificans*: redundant or subtly different in function? J Bacteriol *183*, 7017-7026.

Ozturk, Y., Lee, D.W., Mandaci, S., Osyczka, A., Prince, R.C., and Daldal, F. (2008). Soluble variants of *Rhodobacter capsulatus* membrane-anchored cytochrome c_y are efficient photosynthetic electron carriers. J Biol Chem *283*, 13964-13972.

Pawlik, G., Kulajta, C., Sachelaru, I., Schroder, S., Waidner, B., Hellwig, P., Daldal, F., and Koch, H.G. (2010). The putative assembly factor CcoH is stably associated with the *cbb*$_3$-type cytochrome oxidase. J Bacteriol *192*, 6378-6389.

Quintana-Cabrera, R., and Soriano, M.E. (2019). ER Stress Priming of Mitochondrial Respiratory suPERKomplex Assembly. Trends Endocrinol Metab *30*, 685-687.

Sakamoto, J., Matsumoto, A., Oobuchi, K., and Sone, N. (1996). Cytochrome *bd*-type quinol oxidase in a mutant of *Bacillus stearothermophilus* deficient in *caa*$_3$-type cytochrome *c* oxidase. FEMS Microbiol Lett *143*, 151-158.

Schneidman-Duhovny, D., Inbar, Y., Nussinov, R., and Wolfson, H.J. (2005). PatchDock and SymmDock: servers for rigid and symmetric docking. Nucleic Acids Res *33*, W363-367.

Slavin, M., and Kalisman, N. (2018). Structural Analysis of Protein Complexes by Cross-Linking and Mass Spectrometry. Methods Mol Biol *1764*, 173-183.

Smith, M.A., Finel, M., Korolik, V., and Mendz, G.L. (2000). Characteristics of the aerobic respiratory chains of the microaerophiles *Campylobacter jejuni* and *Helicobacter pylori*. Arch Microbiol *174*, 1-10.

Solmaz, S.R., and Hunte, C. (2008). Structure of complex III with bound cytochrome *c* in reduced state and definition of a minimal core interface for electron transfer. J Biol Chem *283*, 17542-17549.

Sone, N., Sekimachi, M., and Kutoh, E. (1987). Identification and properties of a quinol oxidase super-complex composed of a bc_1 complex and cytochrome oxidase in the thermophilic bacterium PS3. J Biol Chem *262*, 15386-15391.

Sousa, J.S., Mills, D.J., Vonck, J., and Kuhlbrandt, W. (2016). Functional asymmetry and electron flow in the bovine respirasome. Elife *5*.

Sousa, J.S., and Vonck, J. (2019). Respiratory supercomplexes III_2IV_2 come into focus. Nat Struct Mol Biol *26*, 87-89.

Stroh, A., Anderka, O., Pfeiffer, K., Yagi, T., Finel, M., Ludwig, B., and Schagger, H. (2004). Assembly of respiratory complexes I, III, and IV into NADH oxidase supercomplex stabilizes complex I in *Paracoccus denitrificans*. J Biol Chem *279*, 5000-5007.

Swierczek, M., Cieluch, E., Sarewicz, M., Borek, A., Moser, C.C., Dutton, P.L., and Osyczka, A. (2010). An electronic bus bar lies in the core of cytochrome bc_1. Science *329*, 451-454.

Turba, A., Jetzek, M., and Ludwig, B. (1995). Purification of *Paracoccus denitrificans* cytochrome c_{552} and sequence analysis of the gene. Eur J Biochem *231*, 259-265.

Valkova-Valchanova, M.B., Saribas, A.S., Gibney, B.R., Dutton, P.L., and Daldal, F. (1998). Isolation and characterization of a two-subunit cytochrome b-c_1 subcomplex from *Rhodobacter capsulatus* and reconstitution of its ubihydroquinone oxidation (Q_o) site with purified Fe-S protein subunit. Biochemistry *37*, 16242-16251.

Verissimo, A.F., Sousa, F.L., Baptista, A.M., Teixeira, M., and Pereira, M.M. (2007). Thermodynamic redox behavior of the heme centers of cbb_3 heme-copper oxygen reductase from *Bradyrhizobium japonicum*. Biochemistry *46*, 13245-13253.

Weyer, K.A., Lottspeich, F., Gruenberg, H., Lang, F., Oesterhelt, D., and Michel, H. (1987). Amino acid sequence of the cytochrome subunit of the photosynthetic reaction centre from the purple bacterium *Rhodopseudomonas viridis*. EMBO J *6*, 2197-2202.

Wikstrom, M., Krab, K., and Sharma, V. (2018). Oxygen Activation and Energy Conservation by Cytochrome *c* Oxidase. Chem Rev *118*, 2469-2490.

Winstedt, L., and von Wachenfeldt, C. (2000). Terminal oxidases of *Bacillus subtilis* strain 168: one quinol oxidase, cytochrome aa_3 or cytochrome *bd*, is required for aerobic growth. J Bacteriol *182*, 6557-6564.

Wiseman, B., Nitharwal, R.G., Fedotovskaya, O., Schafer, J., Guo, H., Kuang, Q., Benlekbir, S., Sjostrand, D., Adelroth, P., Rubinstein, J.L., *et al*. (2018). Structure of a functional obligate complex III_2IV_2 respiratory supercomplex from *Mycobacterium smegmatis*. Nat Struct Mol Biol *25*, 1128-1136.

Wu, M., Gu, J., Guo, R., Huang, Y., and Yang, M. (2016). Structure of Mammalian Respiratory Supercomplex $I_1III_2IV_1$. Cell *167*, 1598-1609 e1510.

Xia, D., Esser, L., Elberry, M., Zhou, F., Yu, L., and Yu, C.A. (2008). The road to the crystal structure of the cytochrome bc_1 complex from the anoxigenic, photosynthetic bacterium *Rhodobacter sphaeroides*. J Bioenerg Biomembr *40*, 485-492.

Yang, J., Yan, R., Roy, A., Xu, D., Poisson, J., and Zhang, Y. (2015). The I-TASSER Suite: protein structure and function prediction. Nat Methods *12*, 7-8.

Yang, J., and Zhang, Y. (2015). Protein Structure and Function Prediction Using I-TASSER. Curr Protoc Bioinformatics *52*, 5 8 1-5 8 15.

Yu, C.A., Wen, X., Xiao, K., Xia, D., and Yu, L. (2002). Inter- and intra-molecular electron transfer in the cytochrome bc_1 complex. Biochim Biophys Acta *1555*, 65-70.

Zeng, H., Wang, S., Zhou, T., Zhao, F., Li, X., Wu, Q., and Xu, J. (2018). ComplexContact: a web server for inter-protein contact prediction using deep learning. Nucleic Acids Res *46*, W432-W437.

Acknowledgments

This work was supported partly by the National Institute of Health grants, GM 38237 to FD, GM123233 to KM, GM110174 and AI118891 to BAG, T32-GM008275 to TV, T32-GM071339 to HJK, and partly by the Division of Chemical Sciences, Geosciences and Biosciences, Office of Basic Energy Sciences of Department of Energy grant DE-FG02-91ER20052 to FD. This research was funded by ISF 1466/18, BSF 2016070, and Ministry of Science and technology 80802 grants to DS. YO was supported by the grant GRK2202-23577276/RTG from DFG, Germany. Data analysis was partly supported by the National Institute of Health grant S10OD023592.

We thank Drs. Saif S. Hasan, Brian G. Pierce and Christian Presley at the Institute for Bioscience and Biotechnology Research (IBBR), University of Maryland, for insightful discussions and invaluable help they provided during this study. SS and FD also thank Vivian Kitainda for her assistance with protein purification and O_2 consumption measurements.

This research was, in part, supported by the National Cancer Institute, National Cryo-EM Facility at the Frederick National Laboratory for Cancer Research under contract HSSN261200800001E. The authors would like to thank Ulrich Baxa, Thomas Edwards and Adam Wier for their support and helpful discussions. Some cryo-EM data were also obtained at the University of Massachusetts Cryo-EM Core Facility, and we thank Drs. Chen Xu, KangKang Song and Kyounghwan Lee for their support. Cryo-EM sample screening and optimization was performed at the Electron Microscopy Resource Laboratory at the Perelman School of Medicine, University of Pennsylvania, and we thank Dr. Sudheer Molugu for his support.

Data deposition

The following *R. capsulatus* structures and the corresponding cryo-EM maps are deposited to PDB and EMDB with the accession codes listed in the table below:

Structure	PDB	map
$CIII_2$	6XI0	EMD-22189
$CIII_2$ c-c	6XKT	EMD-22224
$CIII_2$ b-c	6XKU	EMD-22225
$CIII_2$ b-b	6XKV	EMD-22226
SC-2A	6XKW	EMD-22227
SC-1A	6XKX	EMD-22228
SC-1B	6XKZ	EMD-22230

The raw XL-MS data deposited to PRIDE repository (http://www.ebi.ac.uk/pride/archive/) with the dataset identifier PXD020038

Table 1: Statistics of data collection and 3D reconstruction of $CIII_2CIV$ SC. Six and two individual datasets were combined for the tripartite (~c_y, fused cyt *c* domain of cyt c_y) and the bipartite (+ c_y, supplemented with native cyt c_y) SCs, respectively. For the combined datasets, the parameters for data collection were identical, except the exposure time. For all combined datasets, the range of exposure times and the corresponding dose rates are provided.

Data Collection		
Sample	**Tripartite $CIII_2CIV$~c_y**	**Bipartite $CIII_2CIV$ + c_y**
Number of micrographs	17390	17680
Electron microscope	FEI Titan Krios	FEI Titan Krios
Voltage (kV)	300	300
Electron detector	K2	K3
Pixel size (Å)	1.32	1.36
Defocus range (μm)	0.4 - 4.0	0.4 - 4.0
Frames per movie	40	80
Total dose ($e^-/Å^2$)	40	40
Exposure time (s)	9 - 15	3.0 - 3.2
Dose rate ($e^-/Å^2 \cdot s^{-1}$)	2.7 - 4.4	12.5 - 13.2
Dose/frame (e^-/pix)	1.74	0.93

3D Reconstruction			
Map Name	**SC–1A**	**SC-1B**	**SC-2A**
Particles	61934	87026	14978
B-factor	-184	-684	-87
Resolution range (Å)	4.5 - 9	4.8 - 9	4.3 – 8
Final resolution (Å) at FSC 0.143 (0.5)	6.09 (7.14)	7.20 (8.85)	5.18 (7.35)
EMDB map entry	EMD-22228	EMD-22230	EMD-22230

Model Refinement			
PDB coordinate entry	6XKX	6XKZ	6XKW
Phenix $CC_{box/mask/volume}$	0.75/0.64/0.64	0.71/0.59/0.58	0.74/0.61/0.63
Refinement statistics	Models were obtained by fitting the high-resolution model of $CIII_2$ (PDB: 6XI0) and the homology model of CIV (**Table S7**) into the maps. See these tables for refinement statistics.		

Table 2: Statistics of 3D reconstruction and model refinement of $CIII_2$. The datasets of the bipartite $CIII_2CIV + c_y$ SC (**Table 1**) were used for the 3D reconstruction of $CIII_2$. The model (PDB: 6XI0) was refined in map $CIII_2$ (EMD-22189) and then used for rigid body fitting in maps $CIII_2$ c-c (EMD-22224), $CIII_2$ b-c (EMD-22225) and $CIII_2$ b-b (EMD-22226).

Data Collection	See Table 1, bipartite $CIII_2CIV + c_y$			
3D Reconstruction				
Map Name	**$CIII_2$**	**$CIII_2$ c-c**	**$CIII_2$ b-c**	**$CIII_2$ b-b**
ED conformation	b – b	c - c	b - c	b - b
Symmetry	C2	C2	C1	C2
Particles	37997	35069	26254	37710
B-factor	-33	-71	-50	-54
Resolution range (Å)	3.0 - 4.0	3.25 - 4.5	3.65 - 5.0	3.0 - 4.0
Final resolution (Å) at FSC 0.143 (0.5)	3.30 (3.70)	3.75 (4.15)	4.18 (4.72)	3.47 (3.89)
Phenix $CC_{box/mask/volume}$	0.70/0.81/0.76	0.74/0.78/0.75	0.74/0.71/0.70	0.70/0.76/0.72
EMDB map entry	EMD-22189	EMD-22224	EMD-22225	EMD-22226
Model Refinement				
PDB coordinate entry	6XI0	6XKT	6XKU	6XKV
Model composition				
Non-hydrogen	13079	13079	13079	13079
atoms	1678	1678	1678	1678
Protein residues	6	6	6	6
Heme groups	2	2	2	2
[2Fe-2S] clusters				
MolProbity Score	2.23	2.28	2.29	2.22
Clash score*	10.59	11.77	12.15	10.21
Rotamer outliers (%)	0.08	0.08	0.16	0.08
C-beta deviations	1	1	1	1
RMSD				
Bond lengths (Å)	0.007	0.008	0.008	0.007
Bond angles (°)	0.971	1.174	1.182	0.976
Ramachandran plot				
Outliers (%)	0.42	0.36	0.30	0.42
Favored (%)	83.17	83.11	83.05	83.17

*Hydrogen atoms were not considered for clash score.

Figure Legends

Figure 1. Schematic representation of fused SCs. A. Oxidation of QH_2 to Q by $CIII_2$ and reduction of O_2 to H_2O by CIV. A bifurcated electron transfer reaction conveys one electron from QH_2 to the [2Fe-2S] cluster of the FeS protein (FeS, yellow), and another electron to hemes b_L and b_H of cyt *b* (periwinkle). The FeS protein transfers the electron from its [2Fe-2S] cluster to heme c_1 on cyt c_1 (green). The movement of reduced FeS protein from heme b_L to heme c_1 and the electron transfer from heme b_H to Q from the pool to form a SQ (semiquinone) are not shown for clarity. An electron carrier cyt *c* (c_2 or c_y) receives the electron from heme c_1 and delivers it to CIV. The electron arriving to CIV reaches the heme-Cu (Cu-b_3) site, where O_2 is reduced to H_2O, via the hemes c_{p1} and c_{p2} of CcoP (P, light blue), c_o of CcoO (O, dark green) and heme *b* of CcoN (N, purple). **B.** *R. capsulatus* genes relevant to the construction of fused SCs. The *petABC* encodes the structural genes of the bc_1-type $CIII_2$ subunits, the FeS protein (*petA*, yellow), cyt *b* (*B*, periwinkle) and cyt c_1 (*C*, green). The *ccoNOQP* encodes the structural genes of the cbb_3-type CIV subunits, the CcoN (*ccoN*, purple), CcoO (*O*, dark green), CcoQ (*Q*, grey) and CcoP (*P*, light blue). The *cycY* gene (red) encodes the membrane-anchored cyt c_y, and its 30-residue transmembrane helix (TMH), 69-residue linker (L) and 100-residue cyt *c* (cyt *c*) domain are indicated. Heme cofactors of *b*- and *c*-type cyts are indicated by black and white asterisks, respectively, and diamond and dot designate the [2Fe-2S] cluster and Cu atom, respectively. **C.** Plasmid-borne genetic fusions. The bipartite fusion (left) is formed by linking in-frame the 3'-end of *petC* to the 5'-end of *ccoP*, and the tripartite fusion (right) is obtained by adding in-frame the linker and cyt *c* domain of *cycY* to the 3'-end of *ccoP*. Colors and cofactor symbols are as in **A**, and the His (H) and Flag (F) affinity tags (dark purple) are added at the 3'-end of the bipartite and tripartite fusion subunits, respectively. **D.** Schematic depiction of bipartite (left) and tripartite (right) super-complexes (SC). The bipartite SC encodes a bc_1-type $CIII_2$ dimer fused on each side to

a His-tagged *cbb*$_3$-type CIV. The tripartite SC also contains the Flag-tagged cyt *c* domain of c_y (red) at the end of CcoP (blue).

Figure 2. Purification and characterization of bipartite and tripartite SCs. The SEC elution profiles of the bipartite SC (**A**) and tripartite SC (**B**) are shown. In each case, the fractions 1 and 2 were analyzed by 4-16% Native PAGE (insets) and silver staining, and only the fractions A-1 and B-1 were used for cryo-EM studies. The bands at ~450/480 kDa corresponding to bipartite and tripartite SCs are indicated by arrows. **C.** Fractions A-1 and B-1 were separated by SDS-PAGE, silver stained, and protein bands identified by mass spectrometry. The fused bipartite c_1-CcoP (A-1) and tripartite c_1-CcoP-c_y (B-1) subunits are indicated by arrows. Note the absence of c_1 and CcoP subunits in both cases. **D**. Peak A-1 and DDM-dispersed membranes from wild type *R. capsulatus* (WT) were analyzed by SDS-PAGE/TMBZ to reveal the covalently attached heme cofactors. The tripartite construct (B-1) is virtually identical to A-1, except that the c_1-CcoP band is replaced by c_1-CcoP-c_y. All *c*-type cyts are labeled, and the additional band indicated by * corresponds to a proteolytic cleavage product of the c_1-CcoP fusion subunit.

Figure 3. Cryo-EM structure of CIII$_2$CIV. A. Side view of CIII$_2$CIV. The structures of CIII$_2$ (PDB: 6XI0, refined in map CIII$_2$ (EMD-22189) starting with PDB: 1ZRT), and the homology model of *cbb*$_3$-type CIV obtained using *P. stutzeri cbb*$_3$ structure (PDB: 3MK7) as a template, were fitted into the cryo-EM map SC-2A depicted in transparent grey. All subunits are colored and labelled as indicated, and the additional feature at the edge of CcoN subunit of CIV, indicated by an arrow, corresponds to the extra N-ter TMH (TMH0, light purple) specific to *R. capsulatus*. The large arrow points out the CcoH/c_y helices in red/blue. **B.** Representative regions of the cryo-EM map showing the map quality and model fitting. The TMH2 and TMH10 of CcoN (left) shows clearly heme *b* and

some bulky side chains. Only the protein backbone and hemes b_L and b_H are resolved between the TMH2 and TMH4 of cyt *b* (center) (see **Fig. 5B** for comparison with $CIII_2$ map at 3.3 Å). Large side chains are clearly visible between the TMH4 of monomer A and TMH4 of monomer B of $CIII_2$ (4_A and 4_B, respectively; right). **C**. Top view of $CIII_2CIV$ TMHs depicted as cylinders and colored as in **A**. The TMHs of cyt *b* (only $CIII_2$ monomer A) and CcoN of CIV are numbered, and the TMHs of the FeS protein (yellow), cyt c_1 (green), CcoO (dark green), CcoP (light blue), CcoH/c_y (blue/red with an arrow) and CcoN TMH0 (light purple) are shown.

Figure 4. Extra features seen in the cryo-EM map of $CIII_2CIV$. A. The $CIII_2CIV$ structure fitted into the map SC-2A (transparent grey) is shown with the same subunit colorings as in **Fig. 3A**, but rotated by 180° for the back view of $CIII_2CIV$ interface. The two extra TMHs at the interface are attributed to those of CcoH (blue) and cyt c_y (red). An additional TMH at the edge of CIV is attributed to the predicted N-ter TMH of CcoN (named TMH0, light purple), and depicted as an *ab initio* model generated by I-TASSER server. **B.** Enlarged view of the region linking CcoN TMH1 (dark purple with N-ter Ser57) to the predicted N-ter TMH0 (light purple). The connection between the two TMHs (dashed line) is not resolved. **C.** Enlarged view of $CIII_2CIV$ interface. The view is slightly rotated relative to **A** for better visibility of CcoP TMH in the background (light blue). For clarity, only CcoN TMH9 is shown next to CcoH (blue) and cyt c_y (red) TMHs. The fusion region between cyt c_1 and CcoP is shown at the bottom, with the C-ter of cyt c_1 (green) and the N-ter (resolved portion in the map) of CcoP (light blue), and their respective terminal residues ($Lys257_{c1}$ and $Thr13_{CcoP}$) are indicated. The 12 N-terminal CcoP residues connecting these two chains (dashed line) are not clearly resolved. **D.** Enlarged view showing close interaction between the CcoH and cyt c_y TMHs. Characteristic features of cyt c_y TMH (NH_2-**Gly11**xxx**Phe15**xxxxx**Tyr21**-COOH) are used to

determine the registration. The helix break induced by Gly11, and the bulky sidechain densities for Phe15 and Tyr21 are clearly visible.

Figure 5: Structures of native $CIII_2$ conformers with their FeS proteins in different positions. **A.** Cryo-EM map $CIII_2$ b-b with both FeS proteins in b position. **B.** Representative region of map $CIII_2$ b-b demonstrating map quality and model fitting. TMH2 and TMH4 of cyt *b* with hemes b_L and b_H are shown. **C-E.** Maps and models showing different conformations of the FeS proteins. In each case, the left panels show the $CIII_2$ structure fitted into the corresponding maps (**Fig. S6F**) with the subunit colorings (cyt *b* in periwinkle, cyt c_1 in green, and the FeS protein in yellow) as in **Fig. 3**. The right panels depict the top half of the models with the membrane-external domain of cyt c_1 omitted for better visibility of the positions (b - b, c – c and c – b) of FeS-EDs, and the [2Fe-2S] clusters are shown as adjacent yellow-red spheres and indicated by arrows. **C.** Structure of native $CIII_2$ with both FeS-EDs in b position (map $CIII_2$ b-b, EMD-22226; PDB: 6XKV). **D.** Structure of native $CIII_2$ with both FeS-EDs in c position (map $CIII_2$ c-c, EMD-22224; PDB: 6XKT). and **E.** Structure of native $CIII_2$ with one FeS-ED in c and one in b position (map $CIII_2$ b-c, EMD-22225; PDB: 6XKU).

Figure 6: Binding regions of cyt c_2 and cyt c_y on $CIII_2CIV$. The binding regions were defined by XL-MS guided docking, and the subunits of $CIII_2CIV$ are colored as in **Fig. 3**, except that the monomer B of $CIII_2$ is shown in light grey for clarity. Only binding regions on monomer A are shown. **A.** Cyt c_2 (PDB: 1C2N) was docked onto $CIII_2$ and CIV using Patchdock with the DMTMM generated XLs as distance restraints, and yielded one cluster of models on CIV and one per monomer of $CIII_2$. **B.** A model of cyt *c* domain of c_y, generated using *P. denitrificans* cyt c_{552} structure (PDB: 3M97) as a template (RMSD between template and model: 0.2 Å) was docked on $CIII_2$ as in **A**, except that both DMTMM and DSBU generated XLs provided distance restraints.

Two binding clusters for cyt *c* domain of c_y per monomer of $CIII_2$ were found. These two clusters are located behind each other on a side view, but they are clearly visible on top views (**Fig. S11C**, labelled 1 and 2). Here, only cluster 1 which is closer to cyt c_1 and overlapping with the binding region of cyt c_2 is shown. In all cases, the top 10 representative models are shown to depict the clusters of binding models. No binding region for cyt c_y on CIV could be defined since no XL was found between these proteins.

Figure 7. Organization of $CIII_2CIV$ cofactors and redox partners. A. The hemes and [2Fe-2S] clusters are shown inside the transparent cryo-EM map SC-2A of $CIII_2CIV$ (EMD-22227) with the same subunit colors as in **Fig. 3**: hemes b_L and b_H (periwinkle), heme c_1 (green), hemes c_{p1} and c_{p2} (light blue), heme c_o (dark green), hemes *b* and b_3 (purple). The [2Fe-2S] clusters are shown as yellow-red spheres. In all cases the distances (heme-Fe to heme-Fe) between the heme cofactors are indicated. The positions of docked cyt c_2 and cyt *c* domain of c_y are indicated as orange (heme c_2) and red (heme c_y) spheres, respectively, representing their heme-Fe atoms. All heme-Fe atoms corresponding to the top 50 docking positions for cyt c_2 on CIV are shown as solid (< 25Å) or transparent (> 25Å) spheres, depending on their distances to heme c_{p2}. In the case of $CIII_2$, only the docking positions of cyt c_2 and cyt c_y on monomer A and between the monomers A and B are shown, omitting those located entirely on monomer B. The TMH of cyt c_y is shown in red at $CIII_2CIV$ interface. **B.** The heme-Fe atoms of all 50 cyt c_2 models docked onto CIV are plotted in function of their distances from the heme c_{p1} and heme c_{p2}, with the Fe atoms within 25Å shown as solid spheres, and those beyond 25Å as transparent spheres, as indicated. The vast majority of heme-Fe atoms of docked cyt c_2 models are closer to heme c_{p2} than heme c_{p1} of CIV (above the diagonal line). **C.** Top view of the map shown in **A** is presented to better visualize the distribution of the docked cyt *c*

domain of c_y on monomer A and between the monomers A and B. In all cases, the heme-Fe atoms are depicted by spheres and colored as indicated above and on the figure.

Figure 8. Proposed cyt c_2 and cyt c_y binding regions of $CIII_2CIV$ and electron transfer pathways. The likely binding regions of cyt c_2 and cyt c domains of c_y (orange and red ellipsoids, respectively), defined by XL-MS guided docking, are depicted by the distributions of their heme-Fe atoms on the transparent map SC-2A of $CIII_2CIV$. Only the positions that are within 25Å of heme c_1 of $CIII_2$ or heme c_{p2} of CIV are indicated. The $CIII_2$ and CIV cofactors together with the TMH of cyt c_y are shown as in **Fig. 7**. The linker region (indicated by dotted or dashed lines) between the TMH and the cyt c domain of c_y is not resolved in the cryo-EM map. The proposed electron transport pathways are shown by thicker black arrows: upon QH_2 oxidation by $CIII_2$, cyt c_y which is integral to $CIII_2CIV$ receives an electron from heme c_1. It then moves (double-headed dashed red arrow) to an undefined binding region (dashed oval with c_y?) on CIV, where it delivers the electron to the nearest heme c_{p1} of CIV. Similarly, cyt c_2 which is peripheral to $CIII_2CIV$ also receives an electron from heme c_1, diffuses away to reach CIV and conveys it to heme c_{p2}. The canonical electron transfers occurring from QH_2 to heme c_1 in $CIII_2$, and from heme c_{p1} to O_2 in CIV, are indicated by thinner arrows. The double headed dashed black arrow depicts the movement of the [2Fe-2S] of FeS protein from the b position (b-pos, in black) to the c position (c-pos, in grey) in $CIII_2$ during QH_2 oxidation. Electron equilibration between the two heme b_L of $CIII_2$ is indicated by double arrows, and the electron transfer steps subsequent to heme b_H reduction are not shown for the sake of clarity.

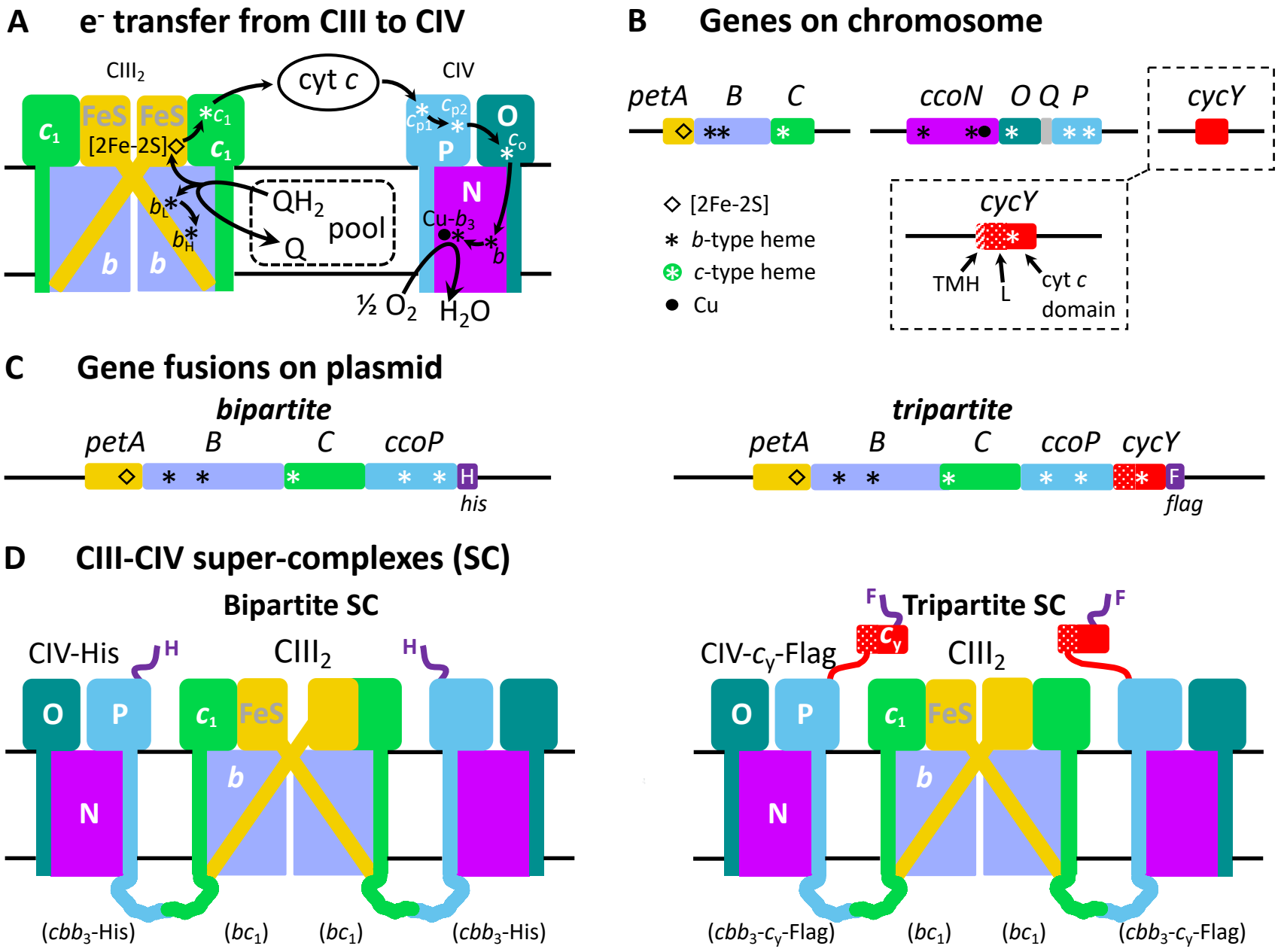

Figure 1. Steimle et al.,

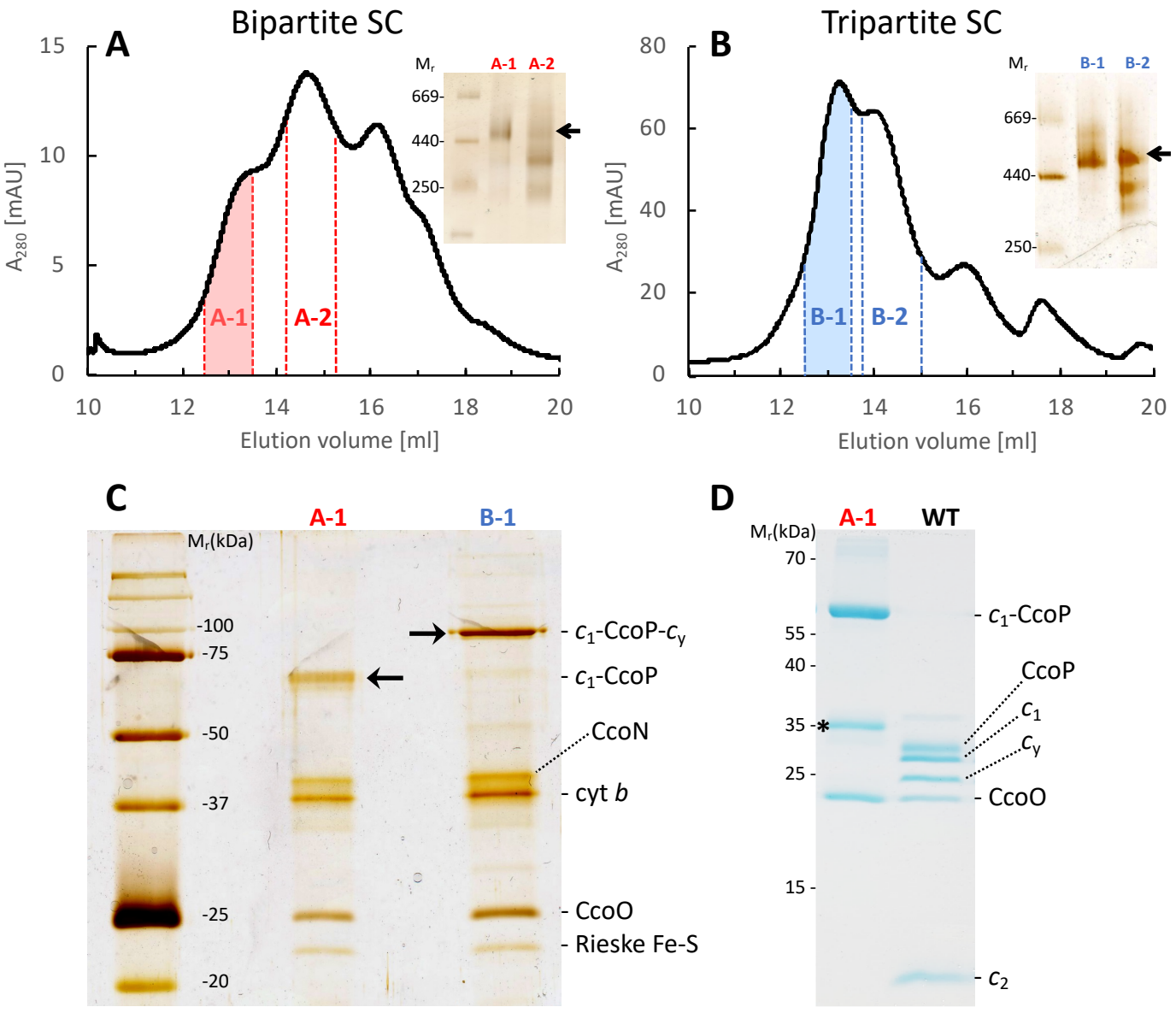

Figure 2. Steimle et al.,

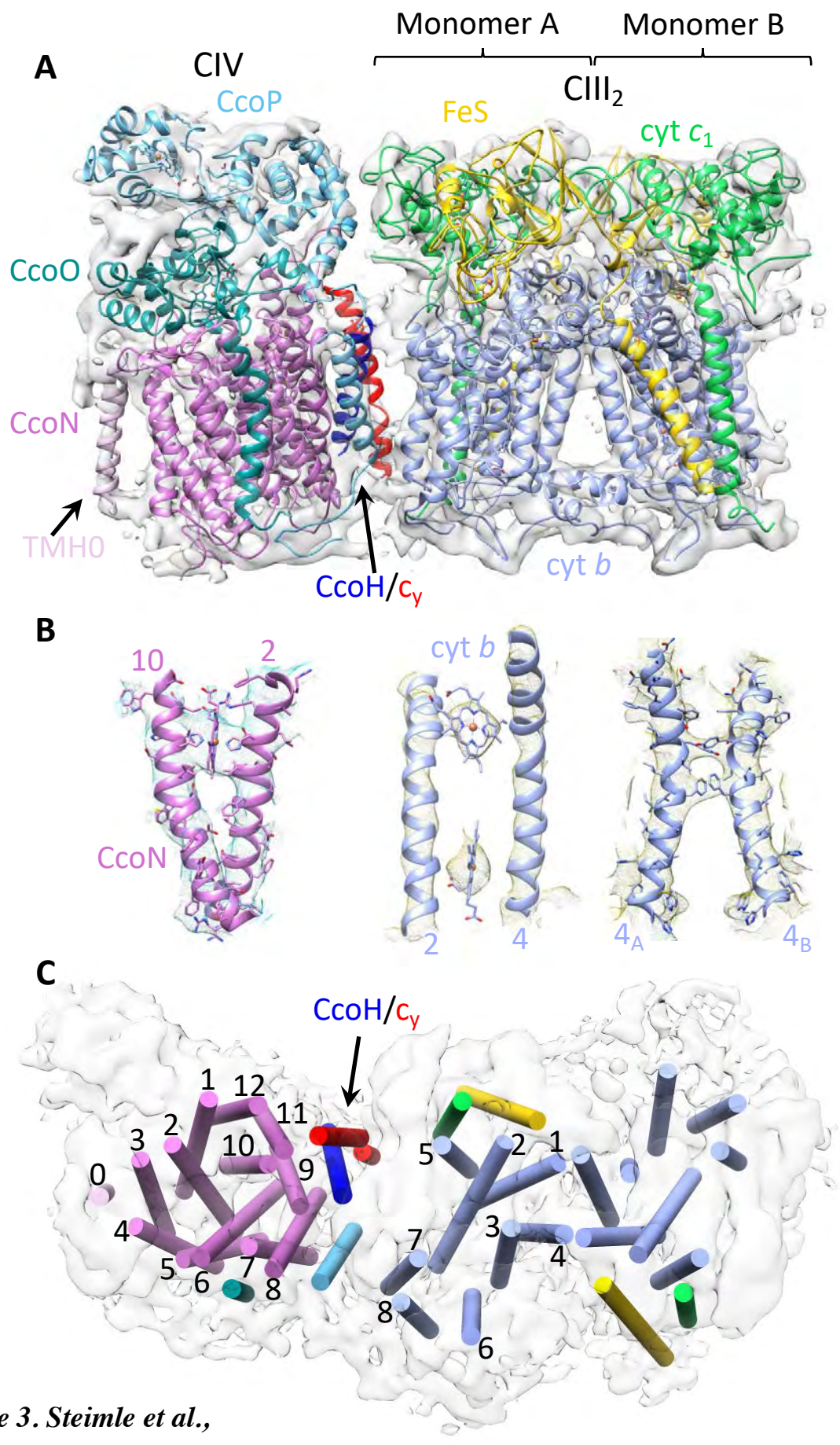

Figure 3. Steimle et al.,

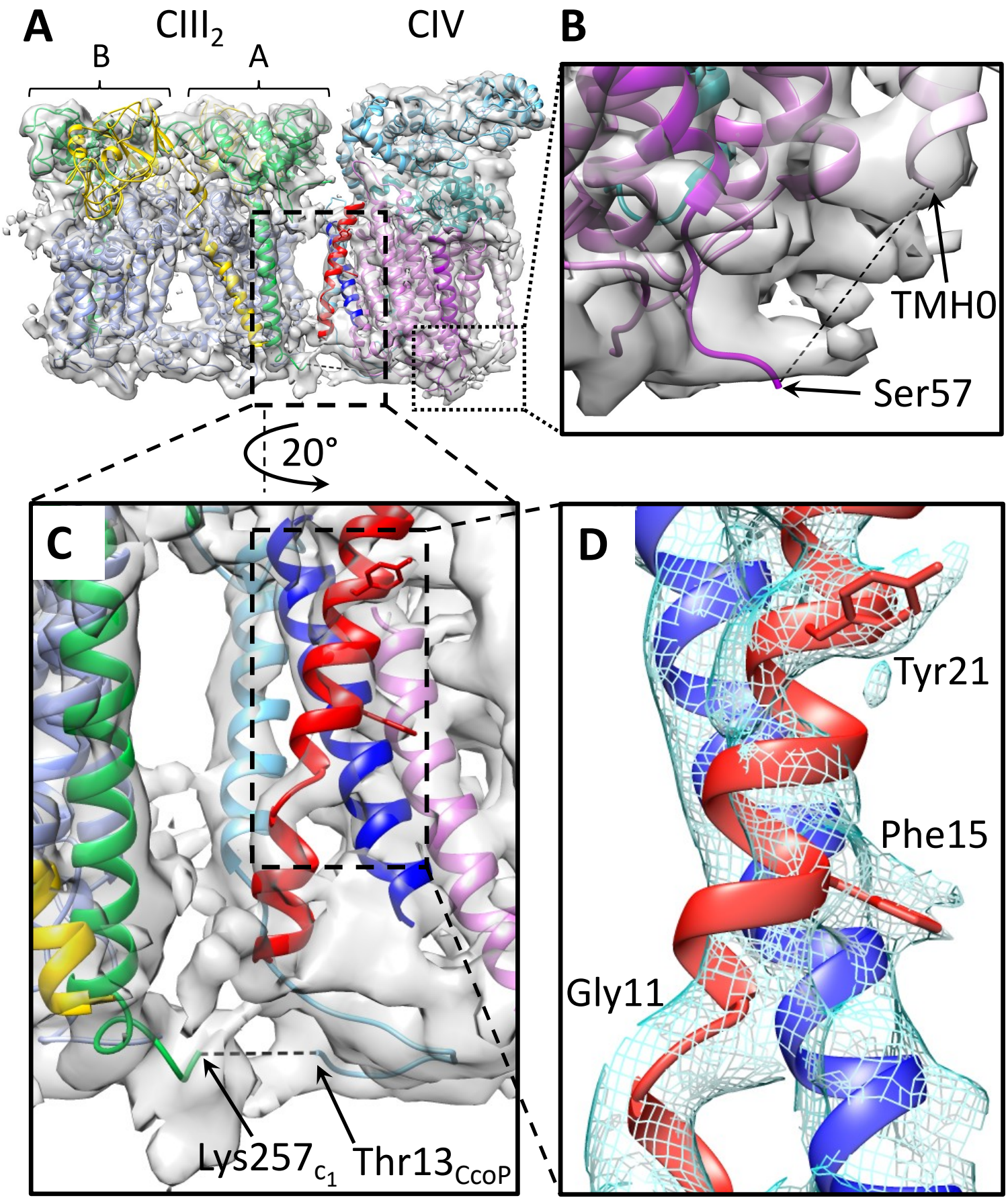

Figure 4, Steimle et al.

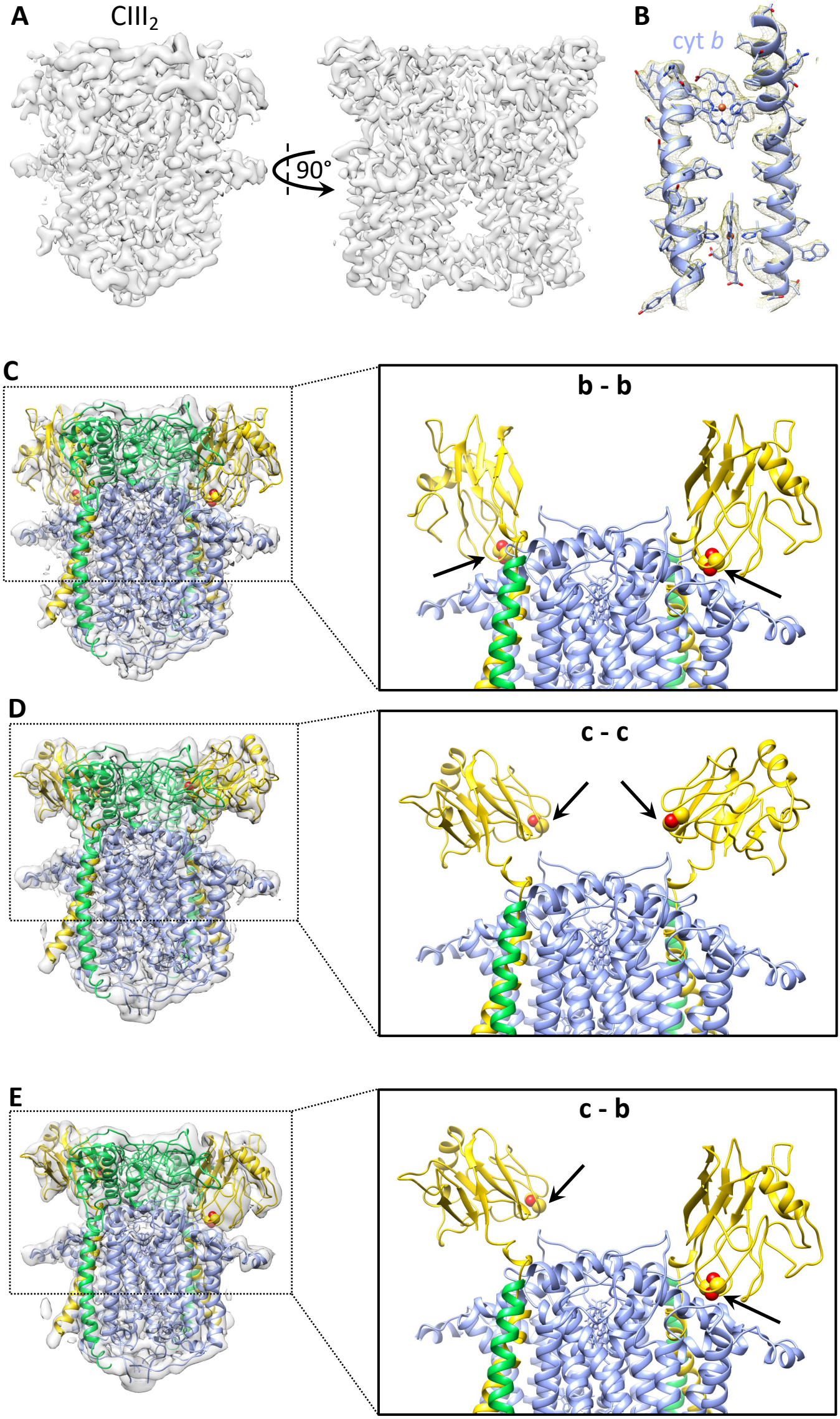

Figure 5. Steimle et al.,

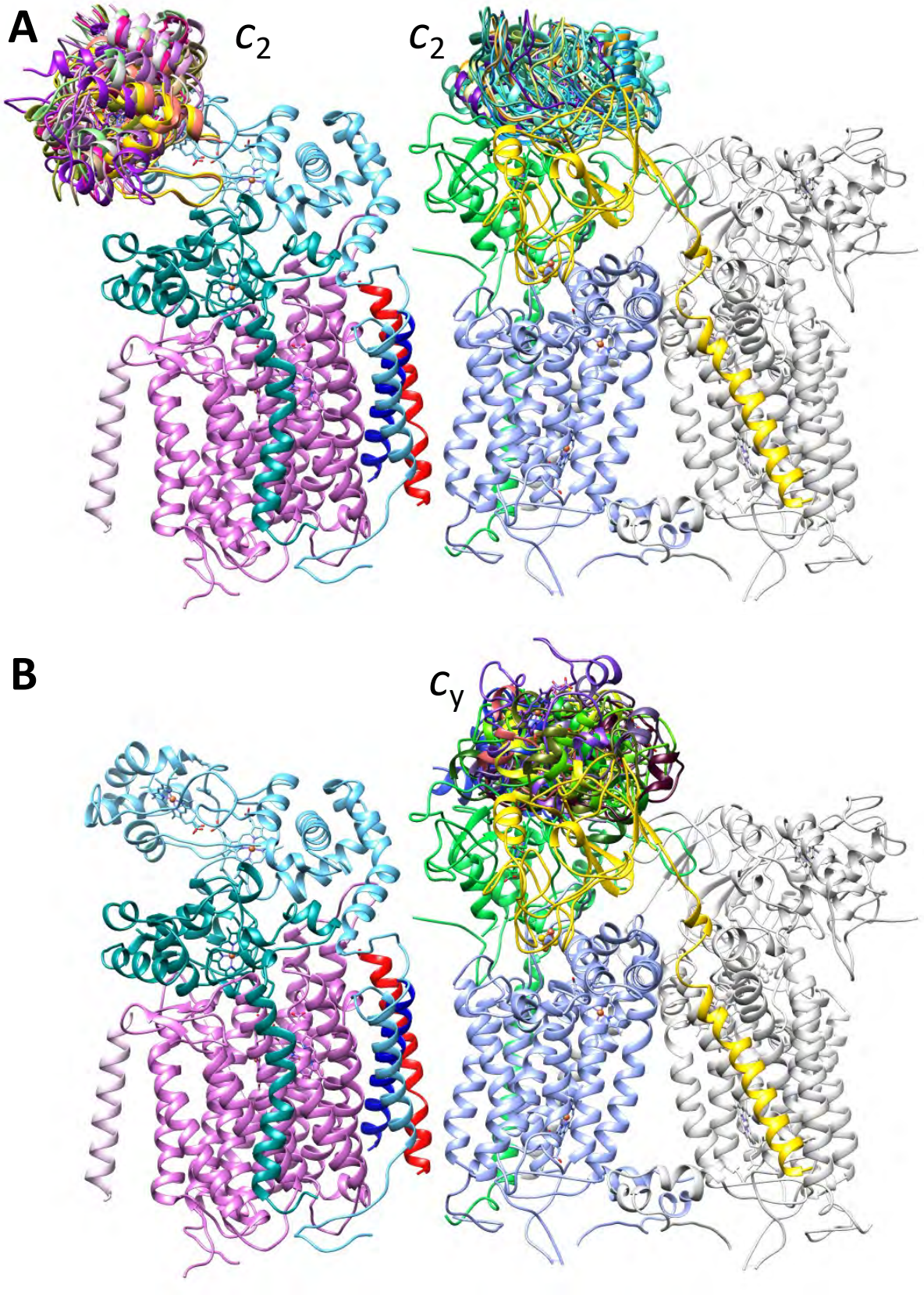

Figure 6. Steimle et al.,

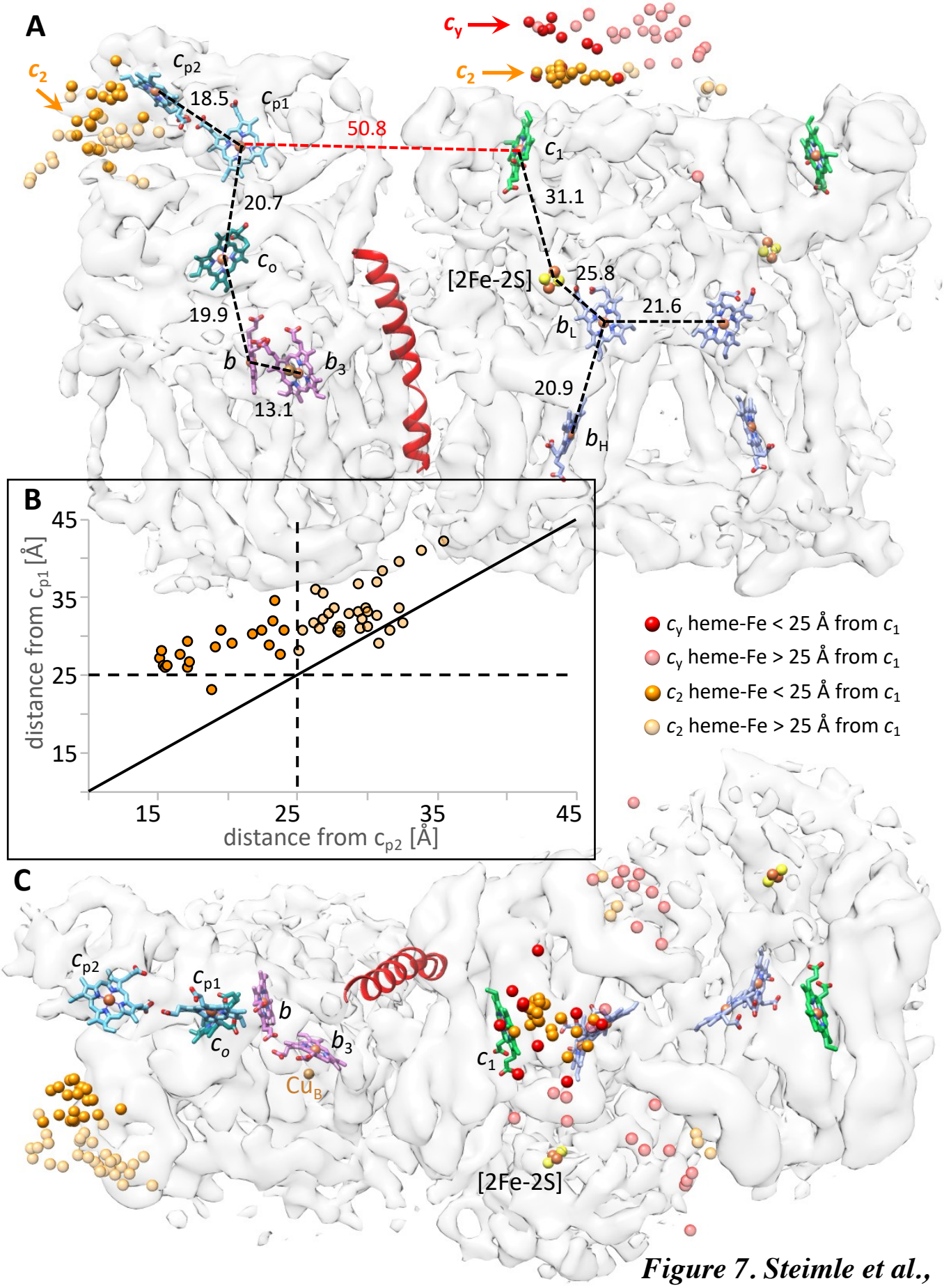

Figure 7. Steimle et al.,

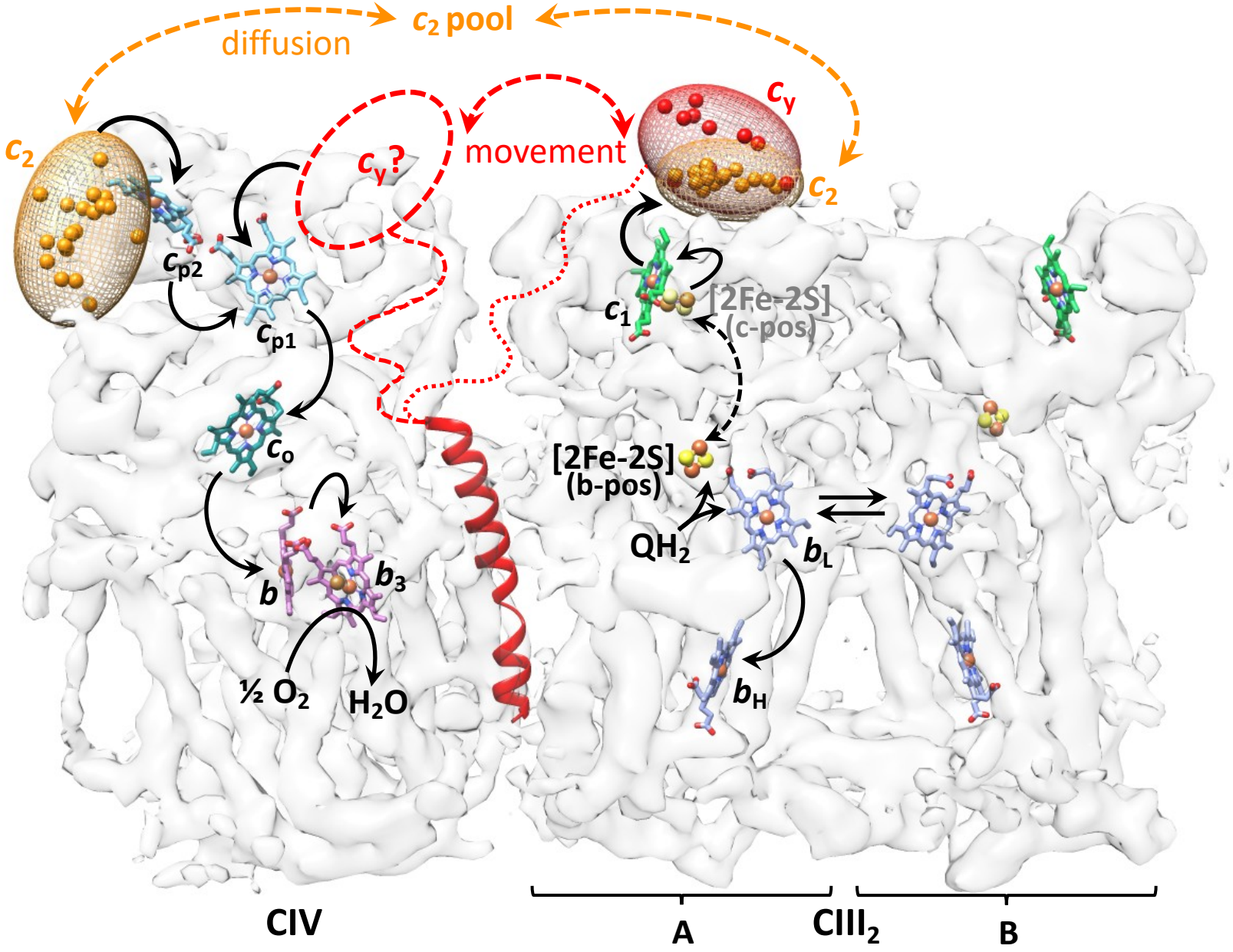

Figure 8. Steimle et al.,